

Contents lists available at ScienceDirect

Journal of Computational Physics

www.elsevier.com/locate/jcp



A second-order time accurate and fully-decoupled numerical scheme of the Darcy-Newtonian-Nematic model for two-phase complex fluids confined in the Hele-Shaw cell



Chuanjun Chen^a, Xiaofeng Yang^{b,*}

- ^a School of Mathematics and Information Sciences, Yantai University, Yantai 264005, China
- ^b Department of Mathematics, University of South Carolina, Columbia, SC, 29208, USA

ARTICLE INFO

Article history: Received 21 February 2021 Received in revised form 30 December 2021 Accepted 27 January 2022 Available online 1 February 2022

Keywords: Hele-Shaw cell Newtonian-Nematic Phase-field Energy stability Second-order Decoupled

ABSTRACT

We consider the numerical approximation of the binary immiscible mixture of nematic liquid crystals and viscous Newtonian fluids confined in a Hele-Shaw cell, where the free interface motion is simulated by using the phase-field approach via the energy variational method. The governing system is highly complicated nonlinear and coupled, consisting of the Darcy equations for the flow field, the Cahn-Hilliard equations for the free moving interface, and the constitutive equation for the nematic liquid crystal. The numerical scheme developed in this paper is the first "ideal" scheme, namely, it not only has the following characteristics: linearity, second-order time accuracy, unconditional energy stability, and decoupling structure, but also at each time step, only needs to solve a few elliptic equations with constant coefficients. We strictly prove that the scheme satisfies the unconditional energy stability and give a detailed implementation process. Various numerical experiments are further carried out to prove the effectiveness of the scheme, in which the influence of the initial orientations and anchoring elastic energy of the liquid crystal on the Saffman-Taylor fingering instability are studied.

© 2022 Elsevier Inc. All rights reserved.

1. Introduction

The binary immiscible mixture of nematic liquid crystals (LCs) and viscous Newtonian fluids has many interesting and important technological applications, such as micro-fluidics, polymer-stabilized liquid crystal, polymer-dispersed liquid crystal technologies, etc. Regarding the mathematical modeling of this mixed material, one of the widely-used modeling methods is to combine the phase-field (diffusive interface) approach with Ericksen-Leslie theory to form a phase-field-director-field model, see [26–28,37,48,51,58,59,62,78–81,85,90] concerning the considerable modeling/analysis/simulations related to this model. The phase-field-director-field model adopts a scalar phase-field variable and a vector director field, where the former represents the labeling function or volume fraction of two fluids, and the latter represents the average orientations of LC molecules. In addition to the energy potentials used to describe the hydrophilic-hydrophobic interaction of the fluid mixture and the classical Ericksen-Leslie formalism for the nematic LCs, two coupled nonlinear potentials are also required, one of which is used to limit the director field variable to one fluid phase using the so-called "weight function" [26,48,51,59,74,78] or the "phase-transition" mechanism [62,85], and the other is used to represent the anchoring of the

E-mail addresses: cjchen@ytu.edu.cn (C. Chen), xfyang@math.sc.edu (X. Yang).

^{*} Corresponding author.

director field along with the fluid interface. Then, by using the gradient flow method (e.g., Cahn-Hilliard dynamics for the phase-field variable and the Allen-Cahn dynamics for the nematic director field) to minimize the free energy, a governing system composed of two highly nonlinear coupled equations for the binary fluid mixture can be obtained.

To simulate the sophisticated free interface motion driven by the flow field (e.g., heart-shaped viscous liquid bubble rising in the nematic fluid, beads-on-string phenomenon of the nematic droplet due to shear flow or gravity, or Saffman-Taylor fingering instability in the Hele-Shaw cell, etc., see [8,9,36,40,58,63,65,74,85,90]), the hydrodynamic equations will be coupled with the phase-field-director-field model to form a full flow-coupled Newtonian-Nematic model. In this paper, we consider numerical approximations of the Newtonian-Nematic model that is confined in the Hele-Shaw cell and focus on the Saffman-Taylor fingering instability of a nematic liquid crystal droplet. The term Hele-Shaw (or Hele-Shaw cell) is often used to describe the restricted movement of fluid between two parallel plates with a small gap. The fluid motion for this type of flow regime conforms to the Darcy's law. For convenience, the Darcy flow coupled Newtonian-Nematic model considered in this paper is referred to as the DNN model for short.

Due to the complex structure of the DNN model involving a large number of coupled nonlinear terms, it is very challenging to design a numerical scheme for solving the model, especially because our goal is to establish a high standard scheme with many ideal characteristics, such as linearity, second-order time accuracy, decoupling structure, and unconditional energy stability (for simplicity, numerical schemes with these properties are called "ideal"). Thus, a natural question arises, how difficult is it to design an "ideal" type scheme for the DNN model? One might think this is not difficult, because there exist many effective numerical methods that can handle the Cahn-Hilliard or Allen-Cahn type equations (e.g., the linear stabilization [43,57,60,77], Invariant Energy Quadratization (IEQ) method [12,68–70,72,75,76], Scalar Auxiliary Variable (SAV) method [13,61,71,73], convex splitting method [33,38,55,66], nonlinear implicit derivative [22], nonlinear quadrature [30,31,52], Exponential Time Differencing (ETD) [21,44], etc.). The "ideal" type scheme may be easily and naturally obtained after stacking these methods together, plus any effective numerical method of the Darcy equation.

However, it is quite the opposite, in fact. The existence of two types of coupling terms makes it extremely difficult to design decoupling schemes. They are (i) advection and surface tension terms, and (ii) the frame invariant time derivative and viscous stress from the LC molecules [29,39,45,46,58,67,84–89]. These terms make the velocity field, director field and phase field variables extremely tightly and nonlinearly coupled together, which brings great challenges to the design of linear and decoupled numerical schemes. So far, to the best of the author's knowledge, there is no "ideal" type of scheme for any flow coupled Newton-Nematic model. The scheme closest to the "ideal" type is constructed in [58,85], which is linear, decoupled and energy stable, but only has first-order time accuracy.

If we take a step back and consider a simpler case, such as the model of Darcy flow coupled with the Cahn-Hilliard equation (nematic LC is omitted), where the difficulty in designing the decoupling scheme only comes from the coupling of advection and surface tension, we notice that there is indeed a scheme with the following characteristics of "decoupling, second-order time accuracy, energy stability" (a partially "ideal" type scheme due to the lack of linearity) was developed in [34,35]. The scheme uses the implicit-explicit combination method to deal with the advection and surface tension terms. By expressing the fluid velocity through pressure and surface tension explicitly, the scheme does achieve a full decoupling structure (see the details introduced in Remark 3.6). However, the method from [34,35] is not extendable. That is, if we apply the method from [34,35] to the DNN model, the flow field in the advection term will involve both the phase-field and the director field variables. This means that although the velocity field might be decoupled from other equations, the price to be paid is that the equations of the phase-field variable and the director field remain coupled. In addition, another disadvantage of this method is that the Cahn-Hilliard equation with variable coefficients must be solved at each time step, which results in a higher computational cost than just solving equations with constant coefficients (see Remark 3.6).

In addition to the coupling of advection and surface tension, the Newtonian-Nematic model also has another unique coupling terms, that is, the frame-invariant time derivatives and the induced viscous stress from the LC molecules. Those terms also bring great challenges to algorithm design. So far, most existing numerical schemes are only suitable for simplified models (that is, these coupling items are completely ignored) as [4,6,32,47,58,84–88], or nonlinear coupling and first-order time accurate as [85], or linear and decoupling, but only have first-order time accuracy as [87,88]. Therefore, to summarize, the current situation is that there is a lack of the effective numerical techniques to discretize these coupled nonlinear terms in the flow-coupled Newtonian-Nematic model to achieve an "ideal" type of scheme.

In this article, for the DNN model, we aim to overcome all above-mentioned numerical challenges and design an "ideal" type scheme. Note that although these coupling items that bring great difficulties to algorithm design have multiple formats, they have a common property, that is, they all satisfy the so-called "zero-energy-contribution" feature. Inspired by this, a nonlocal variable and a special ordinary differential equation (ODE), which consists of the inner products of these coupling terms and some specific variables, are introduced to reformulate the system to an equivalent one. Although the additional ODE at the continuous level is trivial which is implied by the "zero-energy-contribution" feature, after discretization, it plays a key role in obtaining unconditional energy stability. This new decoupling technique, together with several other effective methods (the projection method of Darcy equation and the quadratization method of nonlinear energy functional) enables us to obtain the "ideal" type of scheme for the DNN model. To the best of the author's knowledge, this scheme is the first one that can obtain decoupling structure, second-order time accuracy, linearity, and unconditionally maintain the energy stability of the flow-coupled Newtonian-Nematic model.

From the perspective of practical implementation, the developed algorithm is also very simple. Using the nonlocal characteristics of the introduced variables, each discrete equation can be decomposed into multiple elliptic sub-equations that

can be solved independently, thereby obtaining a fully decoupled method. Not only that, all the obtained sub-equations are linear elliptic equations with constant coefficients, which verifies the high efficiency of the scheme. We also prove the unconditional energy stability as well as the solvability of each step. To demonstrate the stability and accuracy numerically, we further simulate various numerical examples, including the Saffman-Taylor fingering instability caused by the continuously injected radial flow or rotating Hele-Shaw cell, where different anchoring conditions can get very different fingering patterns.

The article is organized as follows. In Section 2, the DNN model is briefly introduced and its law of energy dissipation is verified. In Section 3, we construct a scheme of "ideal" type and describe its implementations in detail. Unconditional energy stability and solvability are also proved rigorously. In Section 4, we perform several accuracy/stability tests and implement various simulations on the Saffman-Taylor fingering instability problems to demonstrate the effectiveness of the scheme. In Section 5, some concluding remarks are given finally.

2. Model equations

Now, we give a brief introduction of the Newtonian-Nematic system ([26,27,62,81,85]) limited to the Hele-Shaw cell, i.e., the DNN model. Suppose that Ω is a smooth, rectangular, open, bounded, connected domain in \mathbb{R}^d , d=2,3. We consider the phase-field model for an immiscible mixture of nematic LC fluid immersed in a viscous fluid matrix where a phase-field variable $\phi(\mathbf{x},t)$ is introduced to denote the volume fraction of the nematic fluid and the viscous fluid, i.e.,

$$\phi = \begin{cases} 1, & \text{Nematic LC fluid,} \\ 0, & \text{Newtonian viscous fluid,} \end{cases}$$
 (2.1)

and a unit vector \mathbf{d} ($|\mathbf{d}| = 1$) is used to denote the director field representing the orientation of the LC molecules. The interface between the LC fluid and the viscous fluid is described by the level set $\{\mathbf{x}: \phi(\mathbf{x},t) = \frac{1}{2}\}$.

The free energy of the Newtonian-Nematic system is postulated as follows,

$$E(\mathbf{d}, \phi) = E_{mix}(\phi) + E_{ela}(\mathbf{d}, \phi) + E_{anch}(\mathbf{d}, \phi), \tag{2.2}$$

and the three energy components of E_{mix} , E_{ela} and E_{anch} are described below.

First, $E_{mix}(\phi)$ is the well-known mixing energy for the binary fluid mixture in the phase-field framework, that reads as

$$E_{mix}(\phi) = \int_{\Omega} \left(\frac{\lambda}{2} |\nabla \phi|^2 + F(\phi)\right) d\mathbf{x},\tag{2.3}$$

where λ is related to the binary fluid interfacial tension, $F(\phi) = \frac{1}{4\epsilon^2}\phi^2(1-\phi)^2$ in the double-well potential that takes $\phi=0$ and $\phi=1$ as two bulk values. The gradient term represents the conformational entropy, promoting material mixing, while the double-well bulk energy density represents the hydrophobic interaction, promoting phase separation. The competition between these two opposing effects allows the coexistence of two distinct phases mediated through a transitional layer whose thickness is controlled by the model parameter ϵ .

Second, E_{ela} is the elastic energy for the nematic LC phase, which takes the Oseen-Frank distortional elastic energy density with one Frank elastic constant approximation ($K_1 = K_2 = K_3 = K$, cf. [23,24,42,58,85,87,88]), that reads as

$$E_{ela}(\mathbf{d}) = \int_{\Omega} \left(\frac{K}{2} |\nabla \mathbf{d}|^2 + \frac{\alpha}{4} |\mathbf{d}|^4 - \frac{\alpha}{2} \frac{\phi - \phi_c}{\phi_c} |\mathbf{d}|^2 \right) d\mathbf{x}, \tag{2.4}$$

where $\phi_c = \frac{1}{2}$, and α is the penalizing parameter. The term $\frac{\phi - \phi_c}{\phi_c}$ is the so-called "phase transition" technique (cf. [62,85]), which is used to restrict the elastic energy of LCs only on $\phi = 1$ (LC phase). When $\phi = 1$ (Nematic phase), the nonlinear bulk potential in (2.4) becomes $\frac{\alpha}{4}(|\mathbf{d}|^2 - 1)^2 - \frac{\alpha}{4}$ that implies $|\mathbf{d}| \to 1$; when $\phi = 0$ (viscous phase), the bulk potential becomes $\frac{\alpha}{4}(|\mathbf{d}|^4 + |\mathbf{d}|^2)$ that implies $|\mathbf{d}| \to 0$.

Third, E_{anch} is the anchoring energy that can accommodate both the parallel and normal anchoring as follows (cf. [26, 27,62,81,85]),

$$E_{anch} = \int_{\Omega} \eta \left(\frac{\gamma}{2} (\mathbf{d} \cdot \nabla \phi)^2 + \frac{1 - \gamma}{2} \left(|\mathbf{d}|^2 |\nabla \phi|^2 - (\mathbf{d} \cdot \nabla \phi)^2 \right) \right) d\mathbf{x}, \tag{2.5}$$

where $\eta > 0$ controls the strength of the anchoring potential. The parameter γ only takes two different values, when $\gamma = 1$ is for parallel anchoring, and $\gamma = 0$ is for normal anchoring, respectively.

Assuming that the fluid motion conforms to the Darcy's law, the DNN model reads as:

$$\mathbf{d}_t + \mathbf{u} \cdot \nabla \mathbf{d} + \frac{1-s}{2} \mathbf{d} \nabla \mathbf{u} - \frac{1+s}{2} \mathbf{d} \cdot \nabla \mathbf{u} = -M_1 \boldsymbol{\omega}, \tag{2.6}$$

$$\boldsymbol{\omega} = -K\Delta \mathbf{d} + \alpha (\mathbf{d} \cdot \mathbf{d}) \mathbf{d} - \alpha \frac{\phi - \phi_c}{\phi_c} \mathbf{d} + \mathbf{W_d}, \tag{2.7}$$

$$\phi_t + \nabla \cdot (\phi \mathbf{u}) = M_2 \Delta \mu, \tag{2.8}$$

$$\mu = -\lambda \Delta \phi + f(\phi) - \frac{\alpha}{2\phi_c} \mathbf{d} \cdot \mathbf{d} + W_{\phi}, \tag{2.9}$$

$$\tau \mathbf{u}_t + \beta \nu(\phi) \mathbf{u} + \nabla p = \omega \nabla \mathbf{d} - \phi \nabla \mu + \nabla \cdot \sigma_e, \tag{2.10}$$

$$\nabla \cdot \mathbf{u} = 0, \tag{2.11}$$

where

$$\begin{cases} \boldsymbol{\omega} = \frac{\delta E(\mathbf{d}, \phi)}{\delta \mathbf{d}}, \mu = \frac{\delta E(\mathbf{d}, \phi)}{\delta \phi}, f(\phi) = F'(\phi) = \frac{1}{\epsilon^2} \phi(\phi - \frac{1}{2})(\phi - 1), \\ \sigma_e = -\frac{1 - s}{2} \mathbf{d} \boldsymbol{\omega} + \frac{1 + s}{2} \boldsymbol{\omega} \mathbf{d}, \\ \mathbf{W}_{\mathbf{d}} = \frac{\delta E_{anch}(\mathbf{d}, \phi)}{\delta \mathbf{d}} = \eta \gamma (\mathbf{d} \cdot \nabla \phi) \nabla \phi + \eta (1 - \gamma) (|\nabla \phi|^2 \mathbf{d} - (\mathbf{d} \cdot \nabla \phi) \nabla \phi), \\ W_{\phi} = \frac{\delta E_{anch}(\mathbf{d}, \phi)}{\delta \phi} = -\eta \gamma \nabla \cdot ((\mathbf{d} \cdot \nabla \phi) \mathbf{d}) + \eta (1 - \gamma) (\nabla \cdot ((\mathbf{d} \cdot \nabla \phi) \mathbf{d}) - \nabla \cdot (|\mathbf{d}|^2 \nabla \phi)), \end{cases}$$
(2.12)

s is a geometry parameter of the liquid crystal molecule [41,85], **u** is the dimensionless seepage velocity, τ is a positive parameter, M_1 , M_2 are two positive mobility parameters, β is the dimensionless hydraulic conductivity, $\nu(\phi) = \nu_1 \phi + \nu_2 (1 - \phi)$ is the fluid viscosity [20], ν_1 and ν_2 are the viscosity for the nematic fluid and the viscous fluid, respectively, p is the pressure, σ_e is the viscous stress tensor due to liquid crystal molecules [11,19,26,41,85,87,88,90].

The equations for **d** and ϕ are derived by taking the variational gradient flow approach for the total free energy in the L^2 and H^{-1} , respectively. In the Darcy equation (2.10), the time derivative of the seepage velocity **u** is retained for flows in Darcy's law, cf. [5,34,35,50]. We consider the following no-flux type boundary conditions, that read as

$$\mathbf{u} \cdot \mathbf{n}|_{\partial\Omega} = \partial_{\mathbf{n}} \psi|_{\partial\Omega} = \partial_{\mathbf{n}} \mu|_{\partial\Omega} = \partial_{\mathbf{n}} \mathbf{d}|_{\partial\Omega} = 0, \tag{2.13}$$

where \mathbf{n} is the outward normal on the boundary.

Remark 2.1. Note that in many works (cf. [11,19,85,87,88]), the three nonlinear terms of the invariant time derivative of the director field $\mathbf{u} \cdot \nabla \mathbf{d} + \frac{1-s}{2} \mathbf{d} \nabla \mathbf{u} - \frac{1+s}{2} \mathbf{d} \cdot \nabla \mathbf{u}$ are often written as an equivalent form of $\mathbf{u} \cdot \nabla \mathbf{d} - \mathbf{W} \cdot \mathbf{d} - s\mathbf{D} \cdot \mathbf{d}$ where $\mathbf{W} = \frac{1}{2} (\nabla \mathbf{u} - (\nabla \mathbf{u})^T)$ is the vorticity tensor and $\mathbf{D} = \frac{1}{2} (\nabla \mathbf{u} + (\nabla \mathbf{u})^T)$ is the rate of strain tensor

 $\mathbf{W} = \frac{1}{2}(\nabla \mathbf{u} - (\nabla \mathbf{u})^T)$ is the vorticity tensor, and $\mathbf{D} = \frac{1}{2}(\nabla \mathbf{u} + (\nabla \mathbf{u})^T)$ is the rate of strain tensor. The time derivatives of any internal variables in continuum mechanics follow the frame indifferent or invariant concerning translation and rigid body rotation. Consequently, the invariant time derivative of the director vector \mathbf{d} contains three parts: (i) the part of material derivative transporting the center of mass: $\mathbf{d}_t + \mathbf{u} \cdot \nabla \mathbf{d}$; (ii) the part rotating the director field due to the fluid vorticity: $-\mathbf{W} \cdot \mathbf{d}$; and (iii) the flow-induced kinematic change of stretching or compressing of the liquid crystal molecules: $-s\mathbf{D} \cdot \mathbf{d}$ (for a flexible/extensible molecule) or $-s\mathbf{D} \cdot \mathbf{d} + s\mathbf{D}$: $\mathbf{d}\mathbf{d}$ (for rigid molecule). As far as the author knows, almost all numerical analyses are based on the simplified version, that is, only the material derivative (i) is considered, while the terms of (ii), (iii), and the stress σ_e are usually omitted due to their highly coupled and nonlinear structure. The author's previous works [85,87,88] attempt to establish numerical schemes for the full flow-coupled director field model. However, the numerical scheme developed in [85,87,88] only has first-order time accuracy, although they have provable energy stability.

It is easy to see that the DNN model (2.6)-(2.11) follows the energy dissipation law by performing the standard process of energy estimate as follows. Some notations are introduced here. We denote the L^2 inner product of any two functions $\phi(\mathbf{x})$ and $\psi(\mathbf{x})$ is denoted by $(\phi, \psi) = \int_{\Omega} \phi(\mathbf{x}) \psi(\mathbf{x}) d\mathbf{x}$, and the L^2 norm of $\phi(\mathbf{x})$ is denoted by $\|\phi\|^2 = (\phi, \phi)$.

Lemma 2.1. The following energy law holds for the DNN system (2.6)-(2.11):

$$\frac{d}{dt}E_{tot}(\phi, \mathbf{d}, \mathbf{u}) = -M_1 \|\omega\|^2 - M_2 \|\nabla \mu\|^2 - \beta \|\sqrt{\nu(\phi)}\mathbf{u}\|^2,$$
(2.14)

where

$$E_{tot}(\phi, \mathbf{d}, \mathbf{u}) = E(\phi, \mathbf{d}) + \frac{\tau}{2} \int_{\Omega} |\mathbf{u}|^2 d\mathbf{x}.$$
 (2.15)

Proof. First, we take the inner product of (2.6) with ω , of (2.7) with $-\mathbf{d}_t$ in L^2 , and combine the two obtained equations to get

$$(\frac{\delta E}{\delta \mathbf{d}}, \mathbf{d}_t) = -M_1 \|\boldsymbol{\omega}\|^2 \underbrace{-(\mathbf{u} \cdot \nabla \mathbf{d}, \boldsymbol{\omega})}_{I_1} \underbrace{-\frac{1-s}{2} (\mathbf{d} \nabla \mathbf{u}, \boldsymbol{\omega})}_{I_{1}} + \underbrace{\frac{1+s}{2} (\mathbf{d} \cdot \nabla \mathbf{u}, \boldsymbol{\omega})}_{IV_1}. \tag{2.16}$$

Second, we take the inner product of (2.8) with μ , of (2.9) with $-\phi_t$ in L^2 , and use integration by parts to get

$$(\frac{\delta E}{\delta \phi}, \phi_t) = -M_2 \|\nabla \mu\|^2 \underbrace{-(\nabla \cdot (\phi \mathbf{u}), \mu)}_{\text{II}_1}. \tag{2.17}$$

Third, we take the inner product of (2.10) with \mathbf{u} in L^2 , and use (2.11) to obtain

$$\frac{d}{dt} \int_{\Omega} \frac{\tau}{2} |\mathbf{u}|^{2} d\mathbf{x} + \beta \|\sqrt{\nu(\phi)}\mathbf{u}\|^{2} = \underbrace{(\boldsymbol{\omega}\nabla\mathbf{d}, \mathbf{u})}_{I_{2}} \underbrace{-(\phi\nabla\mu, \mathbf{u})}_{II_{2}} \\
\underbrace{-\frac{1-s}{2}(\nabla\cdot(\mathbf{d}\boldsymbol{\omega}), \mathbf{u})}_{III_{2}} + \underbrace{\frac{1+s}{2}(\nabla\cdot(\boldsymbol{\omega}\mathbf{d}), \mathbf{u})}_{IV_{2}}.$$
(2.18)

Combining (2.16)-(2.18), we derive the energy law (2.14). \Box

Remark 2.2. From the derivation of the energy law (2.14), we find that all nonlinear integrals labeled by the same Roman numerals are canceled out, namely,

$$I_1 + I_2 = 0$$
, $II_1 + II_2 = 0$, $III_1 + III_2 = 0$, $IV_1 + IV_2 = 0$, (2.19)

which are derived by using the integration by parts and the boundary conditions for \mathbf{u} (note that the last two equalities also use the two identities: $-(\mathbf{d}\nabla\mathbf{u}, \boldsymbol{\omega}) + (\mathbf{d}\boldsymbol{\omega}, \nabla\mathbf{u}) = 0$, $(\mathbf{d} \cdot \nabla\mathbf{u}, \boldsymbol{\omega}) - (\boldsymbol{\omega}\mathbf{d}, \nabla\mathbf{u}) = 0$). These equations can be regarded as the contribution of all these nonlinear terms to the total free energy of the system is zero. This unique "zero-energy-contribution" property [14,69–73,82] will be used to design decoupling type numerical schemes in the next section.

3. Numerical scheme

In this section, we need to design special numerical techniques to linearize and decouple a large number of coupling and nonlinear terms in the DNN system to obtain an "ideal" type numerical scheme, including the advection, the surface tension, the frame invariant derivative, the viscous stress, the nonlinear cubic term $f(\phi)$, the phase transition term, the anchoring coupling potential, and the linear coupling between velocity and pressure through the divergence-free condition.

3.1. Reformulated equivalent system and energy law

We introduce a nonlocal variable Q(t) (see also [70]) and design an ODE system for it, that reads as:

$$\begin{cases}
Q_{t} = (\mathbf{u} \cdot \nabla \mathbf{d}, \boldsymbol{\omega}) - (\boldsymbol{\omega} \nabla \mathbf{d}, \mathbf{u}) + (\nabla \cdot (\boldsymbol{\phi} \mathbf{u}), \boldsymbol{\mu}) + (\boldsymbol{\phi} \nabla \boldsymbol{\mu}, \mathbf{u}) \\
+ \frac{1 - s}{2} (\mathbf{d} \nabla \mathbf{u}, \boldsymbol{\omega}) + \frac{1 - s}{2} (\nabla \cdot (\mathbf{d} \boldsymbol{\omega}), \mathbf{u}) \\
- \frac{1 + s}{2} (\mathbf{d} \cdot \nabla \mathbf{u}, \boldsymbol{\omega}) - \frac{1 + s}{2} (\nabla \cdot (\boldsymbol{\omega} \mathbf{d}), \mathbf{u}), \\
Q_{|t=0} = 1,
\end{cases} (3.1)$$

where **u** satisfies the boundary conditions of the DNN system (2.6)-(2.11). From Remark (2.2), it is easy to see that the ODE (3.1) is the same as a trivial ODE: $Q_t = 0$, $Q_{t=0} = 1$ with the exact solution of Q(t) = 1.

We further define a nonlocal variable U(t) (see also in [68]) as

$$U = \sqrt{\int_{\Omega} N(\phi, \mathbf{d}) d\mathbf{x} + B},\tag{3.2}$$

where

$$N(\phi, \mathbf{d}) = F(\phi) + \frac{\alpha}{4} |\mathbf{d}|^4 - \frac{\alpha}{2} \frac{\phi - \phi_c}{\phi_c} |\mathbf{d}|^2 + \eta \left(\frac{\gamma}{2} (\mathbf{d} \cdot \nabla \phi)^2 + \frac{1 - \gamma}{2} (|\mathbf{d}|^2 |\nabla \phi|^2 - (\mathbf{d} \cdot \nabla \phi)^2) \right),$$
(3.3)

B is a constant to guarantee the radicand always be positive (note that $N(\phi, \mathbf{d})$ is bounded from below, so the constant *B* always exists).

Using the two new variables Q and U, we rewrite the original system (2.6)-(2.11) to the following:

$$\mathbf{d}_t + Q\mathbf{u} \cdot \nabla \mathbf{d} + \frac{1-s}{2} Q\mathbf{d} \nabla \mathbf{u} - \frac{1+s}{2} Q\mathbf{d} \cdot \nabla \mathbf{u} = -M_1 \omega, \tag{3.4}$$

$$\boldsymbol{\omega} = -K\Delta \mathbf{d} + HU,\tag{3.5}$$

$$\phi_t + Q \nabla \cdot (\phi \mathbf{u}) = M_2 \Delta \mu, \tag{3.6}$$

$$\mu = -\lambda \Delta \phi + RU,\tag{3.7}$$

$$U_t = \frac{1}{2}(\mathbf{H}, \mathbf{d}_t) + \frac{1}{2}(R, \phi_t), \tag{3.8}$$

$$\tau \mathbf{u}_t + \beta \nu(\phi) \mathbf{u} + \nabla p = Q \boldsymbol{\omega} \nabla \mathbf{d} - Q \phi \nabla \mu - \frac{1-s}{2} Q \nabla \cdot (\mathbf{d}\boldsymbol{\omega}) + \frac{1+s}{2} Q \nabla \cdot (\boldsymbol{\omega} \mathbf{d}), \tag{3.9}$$

$$\nabla \cdot \mathbf{u} = 0, \tag{3.10}$$

$$Q_{t} = (\mathbf{u} \cdot \nabla \mathbf{d}, \boldsymbol{\omega}) - (\boldsymbol{\omega} \nabla \mathbf{d}, \mathbf{u}) + (\nabla \cdot (\mathbf{u}\phi), \boldsymbol{\mu}) + (\phi \nabla \boldsymbol{\mu}, \mathbf{u})$$

$$+ \frac{1-s}{2} (\mathbf{d} \nabla \mathbf{u}, \boldsymbol{\omega}) + \frac{1-s}{2} (\nabla \cdot (\mathbf{d}\boldsymbol{\omega}), \mathbf{u}) - \frac{1+s}{2} (\mathbf{d} \cdot \nabla \mathbf{u}, \boldsymbol{\omega}) - \frac{1+s}{2} (\nabla \cdot (\boldsymbol{\omega}\mathbf{d}), \mathbf{u}),$$
(3.11)

where

$$\mathbf{H} = \frac{\alpha(\mathbf{d} \cdot \mathbf{d})\mathbf{d} - \alpha \frac{\phi - \phi_c}{\phi_c}\mathbf{d} + \mathbf{W_d}}{\sqrt{\int_{\Omega} N(\phi, \mathbf{d})d\mathbf{x} + B}}, R = \frac{f(\phi) - \frac{\alpha}{2\phi_c}\mathbf{d} \cdot \mathbf{d} + W_{\phi}}{\sqrt{\int_{\Omega} N(\phi, \mathbf{d})d\mathbf{x} + B}}.$$

The transformed system (3.4)-(3.11) satisfies the following initial conditions,

$$(\mathbf{u}, p, \phi, \mathbf{d})|_{t=0} = (\mathbf{u}^0, p^0, \phi^0, \mathbf{d}^0), \ Q|_{t=0} = 1, \ U|_{t=0} = \sqrt{\int_{\Omega} N(\phi^0, \mathbf{d}^0) d\mathbf{x} + B}.$$
(3.12)

Remark 3.1. In (3.4)-(3.11), we can see that the terms associated with the ODE (3.1) are multiplied with Q. Since the nonlocal variable Q(t) is equal to 1, the PDE system will not be changed by this modification. Meanwhile, the three new equations ((3.5), (3.7), (3.8)) are equivalent to the two original equations ((2.7), (2.9)). Therefore, the two PDE systems, (3.4)-(3.11) and (2.6)-(2.11) are equivalent.

We also give the process on how the reformulated equivalent system retains the law of energy dissipation, as shown below.

Lemma 3.1. The reformulated equivalent system (3.4)-(3.11) also follows an energy dissipative law as

$$\frac{d}{dt}\hat{E}_{tot}(\phi, \mathbf{d}, \mathbf{u}, Q, U) = -M_1 \|\boldsymbol{\omega}\|^2 - M_2 \|\nabla \mu\|^2 - \beta \|\sqrt{\nu(\phi)}\mathbf{u}\|^2,$$
(3.13)

where $\hat{E}_{tot}(\phi, \mathbf{d}, \mathbf{u}, Q, U) = \int_{\Omega} \left(\frac{\tau}{2} |\mathbf{u}|^2 + \frac{K}{2} |\nabla \mathbf{d}|^2 + \frac{\lambda}{2} |\nabla \phi|^2 \right) d\mathbf{x} + |U|^2 + \frac{1}{2} |Q|^2 - B.$

Proof. By taking the inner product of (3.4) with ω , we get

$$(\mathbf{d}_{t}, \boldsymbol{\omega}) = -M_{1} \|\boldsymbol{\omega}\|^{2} \underbrace{-Q(\mathbf{u} \cdot \nabla \mathbf{d}, \boldsymbol{\omega})}_{\mathcal{A}_{1}} \underbrace{-\frac{1-s}{2} Q(\mathbf{d} \nabla \mathbf{u}, \boldsymbol{\omega})}_{\mathcal{E}_{t}} + \underbrace{\frac{1+s}{2} Q(\mathbf{d} \cdot \nabla \mathbf{u}, \boldsymbol{\omega})}_{\mathcal{E}_{t}}.$$
(3.14)

By taking the L^2 inner product of (3.5) with $-\mathbf{d}_t$, we get

$$-(\boldsymbol{\omega}, \mathbf{d}_t) = -\frac{d}{dt} \int_{\Omega} \frac{K}{2} |\nabla \mathbf{d}|^2 d\mathbf{x} \underbrace{-U(\mathbf{H}, \mathbf{d}_t)}_{\mathcal{I}_1}.$$
(3.15)

By taking the inner product of (3.6) with μ , we get

$$(\phi_t, \mu) = -M_2 \|\nabla \mu\|^2 \underbrace{-Q\left(\nabla \cdot (\phi \mathbf{u}), \mu\right)}_{\mathcal{B}_1}.$$
(3.16)

By taking the inner product of (3.7) with $-\phi_t$ in L^2 , and use integration by parts to get

$$-(\mu, \phi_t) = -\frac{d}{dt} \int_{\Omega} \frac{\lambda}{2} |\nabla \phi|^2 d\mathbf{x} \underbrace{-U(R, \phi_t)}_{\mathcal{I}_2}.$$
(3.17)

By multiplying (3.8) with 2U, we obtain

$$\frac{d}{dt}|U|^2 = \underbrace{U(\mathbf{H}, \mathbf{d}_t) + U(R, \phi_t)}_{\mathcal{I}_3}.$$
(3.18)

By taking the inner product of (3.9) with \mathbf{u} in L^2 , and use (3.10) to obtain

$$\frac{d}{dt} \int_{\Omega} \frac{\tau}{2} |\mathbf{u}|^{2} d\mathbf{x} + \beta \|\sqrt{\nu(\phi)}\mathbf{u}\|^{2} = \underbrace{Q(\omega \nabla \mathbf{d}, \mathbf{u})}_{C_{1}} \underbrace{-Q(\phi \nabla \mu, \mathbf{u})}_{D_{1}} \\
\underbrace{-\frac{1-s}{2} Q(\nabla \cdot (\mathbf{d}\omega), \mathbf{u})}_{G_{1}} + \underbrace{\frac{1+s}{2} Q(\nabla \cdot (\omega \mathbf{d}), \mathbf{u})}_{\mathcal{H}_{1}}.$$
(3.19)

By multiplying (3.11) with Q, we obtain

$$\frac{d}{dt} \left(\frac{1}{2} |Q|^{2} \right) = \underbrace{\underbrace{Q \left(\mathbf{u} \cdot \nabla \mathbf{d}, \boldsymbol{\omega} \right)}_{A_{2}} \underbrace{-Q \left(\boldsymbol{\omega} \nabla \mathbf{d}, \mathbf{u} \right)}_{C_{2}} + \underbrace{\underbrace{Q \left(\nabla \cdot \left(\mathbf{u} \boldsymbol{\phi} \right), \mu \right)}_{B_{2}} + \underbrace{\underbrace{Q \left(\boldsymbol{\phi} \nabla \mu, \mathbf{u} \right)}_{D_{2}}}_{D_{2}} + \underbrace{\underbrace{\frac{1-s}{2} Q \left(\mathbf{d} \nabla \mathbf{u}, \boldsymbol{\omega} \right)}_{\mathcal{E}_{2}} + \underbrace{\frac{1-s}{2} Q \left(\nabla \cdot \left(\mathbf{d} \boldsymbol{\omega} \right), \mathbf{u} \right)}_{\mathcal{G}_{2}} - \underbrace{\underbrace{\frac{1+s}{2} Q \left(\mathbf{d} \cdot \nabla \mathbf{u}, \boldsymbol{\omega} \right)}_{\mathcal{F}_{2}} - \underbrace{\frac{1+s}{2} Q \left(\nabla \cdot \left(\boldsymbol{\omega} \mathbf{d} \right), \mathbf{u} \right)}_{\mathcal{H}_{2}}.$$
(3.20)

Combining (3.14)-(3.20), we derive the law of energy dissipation (3.13) since all terms underbraced by same letters are canceled. \Box

Remark 3.2. The difference between Lemma 2.1 and Lemma 3.1 in the process of deriving the law of energy dissipation fully explains why the original system (2.6)-(2.11) is converted to a new equivalent form (3.4)-(3.11). Taking the advection term $\nabla \cdot (\phi \mathbf{u})$ in (2.8) as an example, when deriving the energy law for the original PDE system (2.6)-(2.11) in Lemma 2.1, we notice that the term I_1 in (2.16) and I_2 in (2.18) must cancel each other, this means the discretization of these two terms must be matched, thereby leading to the coupled type schemes. While for the newly modified system (3.4)-(3.11), the term \mathcal{B}_1 in (3.16) and \mathcal{D}_1 in (3.19) are not necessary to cancel with each other, since the term \mathcal{B}_2 in (3.20) can cancel \mathcal{B}_1 , and the term \mathcal{D}_2 in (3.20) can cancel \mathcal{D}_1 . In other words, when developing numerical schemes, we can use different discretization methods to deal with the term $\mathcal{Q} \nabla \cdot (\phi \mathbf{u})$ in (3.6) and the term $-\mathcal{Q} \phi \nabla \mu$ in (3.9), thereby making it possible to construct a full decoupling type scheme.

3.2. Numerical scheme

We are now ready to develop the "ideal" type time marching numerical scheme to solve the transformed system (3.4)-(3.11). Let $\delta t > 0$ be a time step size and set $t^n = n\delta t$ for $0 \le n \le N$ with $T = N\delta t$. Let ψ^n be the numerical approximation to the analytic function $\psi(\cdot,t)|_{t=t^n}$.

Using the second-order backward differentiation formula for the time derivative, the numerical scheme for solving the system (3.4)-(3.11) reads as follows. Assuming that $(\mathbf{d}, \phi, \omega, \mu, \mathbf{u}, p, Q, U)^{n-1}$ and $(\mathbf{d}, \phi, \omega, \mu, \mathbf{u}, p, Q, U)^n$ are known, we calculate $(\mathbf{d}, \phi, \omega, \mu, \mathbf{u}, p, Q, U)^{n+1}$ as follows.

$$\frac{a\mathbf{d}^{n+1} - b\mathbf{d}^n + c\mathbf{d}^{n-1}}{2\delta t} = -M_1 \boldsymbol{\omega}^{n+1} - Q^{n+1} \mathbf{u}^* \cdot \nabla \mathbf{d}^* - \frac{1-s}{2} Q^{n+1} \mathbf{d}^* \nabla \mathbf{u}^* + \frac{1+s}{2} Q^{n+1} \mathbf{d}^* \cdot \nabla \mathbf{u}^*, \tag{3.21}$$

$$\boldsymbol{\omega}^{n+1} = -K \Delta \mathbf{d}^{n+1} + \mathbf{H}^* U^{n+1} + C(\mathbf{d}^{n+1} - \mathbf{d}^*), \tag{3.22}$$

$$\frac{a\phi^{n+1} - b\phi^n - c\phi^{n-1}}{2\delta t} + Q^{n+1}\nabla \cdot (\phi^* \mathbf{u}^*) = M_2 \Delta \mu^{n+1}, \tag{3.23}$$

$$\mu^{n+1} = -\lambda \Delta \phi^{n+1} + R^* U^{n+1} + \frac{S_1}{\epsilon^2} (\phi^{n+1} - \phi^*) - S_2 \Delta (\phi^{n+1} - \phi^*), \tag{3.24}$$

$$aU^{n+1} - bU^{n} - cU^{n-1} = \frac{1}{2} (\mathbf{H}^{*}, a\mathbf{d}^{n+1} - b\mathbf{d}^{n} + c\mathbf{d}^{n-1})$$

$$+ \frac{1}{2} (R^{*}, a\phi^{n+1} - b\phi^{n} + c\phi^{n-1}),$$
(3.25)

$$\tau \frac{a\tilde{\mathbf{u}}^{n+1} - b\mathbf{u}^n + c\mathbf{u}^{n-1}}{2\delta t} + \beta \nu (\hat{\boldsymbol{\phi}}^*)\tilde{\mathbf{u}}^{n+1} + \nabla p^n = Q^{n+1}\boldsymbol{\omega}^* \nabla \mathbf{d}^* - Q^{n+1}\boldsymbol{\phi}^* \nabla \mu^*$$

$$-\frac{1-s}{2}Q^{n+1}\nabla \cdot (\mathbf{d}^*\boldsymbol{\omega}^*) + \frac{1+s}{2}Q^{n+1}\nabla \cdot (\boldsymbol{\omega}^*\mathbf{d}^*),$$
(3.26)

$$\frac{aQ^{n+1} - bQ^{n} + cQ^{n-1}}{2\delta t} = (\mathbf{u}^* \cdot \nabla \mathbf{d}^*, \boldsymbol{\omega}^{n+1}) - (\boldsymbol{\omega}^* \nabla \mathbf{d}^*, \tilde{\mathbf{u}}^{n+1}) \\
+ (\nabla \cdot (\mathbf{u}^* \boldsymbol{\phi}^*), \boldsymbol{\mu}^{n+1}) + (\boldsymbol{\phi}^* \nabla \boldsymbol{\mu}^*, \tilde{\mathbf{u}}^{n+1}) \\
+ \frac{1 - s}{2} (\mathbf{d}^* \nabla \mathbf{u}^*, \boldsymbol{\omega}^{n+1}) + \frac{1 - s}{2} (\nabla \cdot (\mathbf{d}^* \boldsymbol{\omega}^*), \tilde{\mathbf{u}}^{n+1}) \\
- \frac{1 + s}{2} (\mathbf{d}^* \cdot \nabla \mathbf{u}^*, \boldsymbol{\omega}^{n+1}) - \frac{1 + s}{2} (\nabla \cdot (\boldsymbol{\omega}^* \mathbf{d}^*), \tilde{\mathbf{u}}^{n+1}),$$
(3.27)

$$\frac{a\tau}{2\delta t}(\mathbf{u}^{n+1} - \tilde{\mathbf{u}}^{n+1}) + \nabla(p^{n+1} - p^n) = 0, \tag{3.28}$$

$$\nabla \cdot \mathbf{u}^{n+1} = 0, \tag{3.29}$$

where

$$\begin{cases} a = 3, b = 4, c = 1, \mathbf{u}^* = 2\mathbf{u}^n - \mathbf{u}^{n-1}, \mathbf{d}^* = 2\mathbf{d}^n - \mathbf{d}^{n-1}, \boldsymbol{\omega}^* = 2\boldsymbol{\omega}^n - \boldsymbol{\omega}^{n-1}, \\ \phi^* = 2\phi^n - \phi^{n-1}, \mu^* = 2\mu^n - \mu^{n-1}, \mathbf{H}^* = \mathbf{H}(\phi^*, \mathbf{d}^*), R^* = R(\phi^*, \mathbf{d}^*), \\ \hat{\phi} = \begin{cases} \phi, & |\phi| < 1, \\ \text{sign}(\phi), & |\phi| > 1, \end{cases} \end{cases}$$
(3.30)

and C, S_1, S_2 are positive stabilization parameters. The boundary conditions are set to be

$$\partial_{\mathbf{n}} \mathbf{d}^{n+1}|_{\partial\Omega} = \mathbf{0}, \ \partial_{\mathbf{n}} \phi^{n+1}|_{\partial\Omega} = \partial_{\mathbf{n}} \mu^{n+1}|_{\partial\Omega} = \mathbf{u}^{n+1} \cdot \mathbf{n}|_{\partial\Omega} = 0. \tag{3.31}$$

Several remarks are in order.

Remark 3.3. The initialization of the BDF2 scheme (3.21)-(3.29) needs the values of all variables at $t=t^1$. These values can be easily obtained by developing any first-order scheme to take one time step forward to obtain values at $t=t^1$. For example, by setting a=b=2, c=0, and $r^*=r^0$ for any variable r for (3.21)-(3.29), the first-order scheme is obtained. Meanwhile, the volume-conserved property of ϕ^{n+1} still holds, which can be proved by taking the L^2 inner product of (3.23) with 1 and applying the math induction since the first-order scheme also conserves the volume.

Remark 3.4. A second-order pressure-correction scheme is used to decouple the computation of the pressure from that of the velocity. $\tilde{\mathbf{u}}^{n+1}$ is the intermediate velocity and \mathbf{u}^{n+1} is the final velocity field that satisfies the divergence-free condition.

Remark 3.5. When the system has very high stiffness issues caused by the model parameters or other conditions, while some numerical methods are formally unconditionally energy stable, to obtain reasonable accuracy, very small time steps are needed, see the stabilized-IEQ/SAV methods in [13,56,61,83]. To fix such an inherent deficiency, a commonly used effective way is to add one or more extra linear stabilization terms with the corresponding temporal order. The stabilization term associated with $\frac{S_1}{\epsilon^2}$ is used to balance the explicit treatment of $f(\phi)$. Therefore, the scale of the splitting error caused by this term is about $\frac{S_1}{\epsilon^2} \delta t^2 \partial_{tt} \phi(\cdot)$, which is consistent with the splitting error caused by the second-order extrapolated nonlinear term $f(\phi)$. Hence $S_1 \sim O(1)$. Similarly, $C \sim \eta$, $S_2 \sim \eta$, and the associated stabilization terms of C and C0 are used to balance the extrapolation of nonlinear terms of C1. In Section 4, we present numerical evidence to show that this stabilizer is effective to improve the energy stability while using large time steps in Fig. 4.1. Similar linear stabilization techniques had been widely used in the numerical scheme for solving the phase-field type models, e.g., the methods of linear stabilization, IEQ, SAV, convex-splitting methods, etc., see [12,13,17,56,57,61,75,83].

We now show that the scheme (3.21)-(3.29) is unconditionally energy stable. We will use the following three identities repeatedly:

$$2(a - b, a) = |a|^2 - |b|^2 + |a - b|^2,$$
(3.32)

$$2(3a - 4b + c)a = |a|^2 - |b|^2 + |2a - b|^2 - |2b - c|^2 + |a - 2b + c|^2,$$
(3.33)

$$(3a - 4b + c)(a - 2b + c) = |a - b|^2 - |b - c|^2 + 2|a - 2b + c|^2.$$
(3.34)

Theorem 3.1. The scheme (3.21)-(3.29) holds an energy dissipation law that reads as

$$\frac{1}{\delta t}(E^{n+1} - E^n) \le -\beta \|\sqrt{\nu(\hat{\phi}^*)}\tilde{\mathbf{u}}^{n+1}\|^2 - M_1\|\boldsymbol{\omega}^{n+1}\|^2 - M_2\|\nabla\mu^{n+1}\|^2 \le 0,$$
(3.35)

where

$$\begin{split} E^{n+1} &= \frac{\tau}{2} \left(\frac{1}{2} \| \mathbf{u}^{n+1} \|^2 + \frac{1}{2} \| 2 \mathbf{u}^{n+1} - \mathbf{u}^n \|^2 \right) + \frac{\lambda}{2} \left(\frac{1}{2} \| \nabla \phi^{n+1} \|^2 + \frac{1}{2} \| 2 \nabla \phi^{n+1} - \nabla \phi^n \|^2 \right) \\ &+ \frac{K}{2} \left(\frac{1}{2} \| \nabla \mathbf{d}^{n+1} \|^2 + \frac{1}{2} \| 2 \nabla \mathbf{d}^{n+1} - \nabla \mathbf{d}^n \|^2 \right) + \left(\frac{1}{2} |U^{n+1}|^2 + \frac{1}{2} |2U^{n+1} - U^n|^2 \right) \\ &+ \frac{1}{2} \left(\frac{1}{2} |Q^{n+1}|^2 + \frac{1}{2} |2Q^{n+1} - Q^n|^2 \right) + \frac{\delta t^2}{3\tau} \| \nabla p^{n+1} \|^2 \\ &+ \frac{S_1}{2\epsilon^2} \| \phi^{n+1} - \phi^n \|^2 + \frac{S_2}{2} \| \nabla (\phi^{n+1} - \phi^n) \|^2 + \frac{C}{2} \| \mathbf{d}^{n+1} - \mathbf{d}^n \|^2. \end{split} \tag{3.36}$$

Proof. We take the inner product of (3.26) with $2\delta t \tilde{\mathbf{u}}^{n+1}$ in the L^2 space to get

$$\tau(3\tilde{\mathbf{u}}^{n+1} - 4\mathbf{u}^{n} + \mathbf{u}^{n-1}, \tilde{\mathbf{u}}^{n+1}) + 2\beta\delta t \|\sqrt{\nu(\hat{\phi}^{*})}\tilde{\mathbf{u}}^{n+1}\|^{2} + 2\delta t(\nabla p^{n}, \tilde{\mathbf{u}}^{n+1})$$

$$= 2\delta t Q^{n+1}(\boldsymbol{\omega}^{*}\nabla \mathbf{d}^{*}, \tilde{\mathbf{u}}^{n+1}) - 2\delta t Q^{n+1}(\phi^{*}\nabla \mu^{*}, \tilde{\mathbf{u}}^{n+1})$$

$$- \frac{1-s}{2}2\delta t Q^{n+1}(\nabla \cdot (\mathbf{d}^{*}\boldsymbol{\omega}^{*}), \tilde{\mathbf{u}}^{n+1})$$

$$+ \frac{1+s}{2}2\delta t Q^{n+1}(\nabla \cdot (\boldsymbol{\omega}^{*}\mathbf{d}^{*}), \tilde{\mathbf{u}}^{n+1}),$$

$$(3.37)$$

where $\nu(\hat{\phi}^*) > \min(\nu_1, \nu_2) > 0$ is from the definition of ϕ^* in (3.30).

From (3.28), for any variable \mathbf{v} with $\mathbf{v} \cdot \mathbf{n}|_{\partial\Omega} = 0$ and $\nabla \cdot \mathbf{v} = 0$, we have

$$(\mathbf{u}^{n+1}, \mathbf{v}) = (\tilde{\mathbf{u}}^{n+1}, \mathbf{v}).$$
 (3.38)

Using (3.38) and (3.33), we derive following equality

$$\tau(3\tilde{\mathbf{u}}^{n+1} - 4\mathbf{u}^{n} + \mathbf{u}^{n-1}, \tilde{\mathbf{u}}^{n+1})
= \tau(3\tilde{\mathbf{u}}^{n+1} - 4\mathbf{u}^{n} + \mathbf{u}^{n-1}, \mathbf{u}^{n+1}) + \tau(3\tilde{\mathbf{u}}^{n+1} - 4\mathbf{u}^{n} + \mathbf{u}^{n-1}, \tilde{\mathbf{u}}^{n+1} - \mathbf{u}^{n+1})
= \tau(3\mathbf{u}^{n+1} - 4\mathbf{u}^{n} + \mathbf{u}^{n-1}, \mathbf{u}^{n+1}) + \tau(3\tilde{\mathbf{u}}^{n+1}, \tilde{\mathbf{u}}^{n+1} - \mathbf{u}^{n+1})
= \tau(3\mathbf{u}^{n+1} - 4\mathbf{u}^{n} + \mathbf{u}^{n-1}, \mathbf{u}^{n+1}) + 3\tau(\tilde{\mathbf{u}}^{n+1} - \mathbf{u}^{n+1}, \tilde{\mathbf{u}}^{n+1} + \mathbf{u}^{n+1})
= \frac{\tau}{2} \Big(\|\mathbf{u}^{n+1}\|^{2} - \|\mathbf{u}^{n}\|^{2} + \|2\mathbf{u}^{n+1} - \mathbf{u}^{n}\|^{2} - \|2\mathbf{u}^{n} - \mathbf{u}^{n-1}\|^{2}
+ \|\mathbf{u}^{n+1} - 2\mathbf{u}^{n} + \mathbf{u}^{n-1}\|^{2} \Big) + 3\tau(\|\tilde{\mathbf{u}}^{n+1}\|^{2} - \|\mathbf{u}^{n+1}\|^{2}).$$
(3.39)

We reformulate the projection step (3.28) as

$$\frac{3\tau}{2\delta t}\mathbf{u}^{n+1} + \nabla p^{n+1} = \frac{3\tau}{2\delta t}\tilde{\mathbf{u}}^{n+1} + \nabla p^{n}.\tag{3.40}$$

By taking the square of both sides of the above equation, we get

$$\frac{9\tau^2}{4\delta t^2} \|\mathbf{u}^{n+1}\|^2 + \|\nabla p^{n+1}\|^2 = \frac{9\tau^2}{4\delta t^2} \|\tilde{\mathbf{u}}^{n+1}\|^2 + \|\nabla p^n\|^2 + \frac{3\tau}{\delta t} (\tilde{\mathbf{u}}^{n+1}, \nabla p^n). \tag{3.41}$$

Hence, by multiplying $\frac{2\delta t^2}{3\tau}$ of the above equation, we derive

$$\frac{3\tau}{2}(\|\mathbf{u}^{n+1}\|^2 - \|\tilde{\mathbf{u}}^{n+1}\|^2) + \frac{2\delta t^2}{3\tau}(\|\nabla p^{n+1}\|^2 - \|\nabla p^n\|^2) = 2\delta t(\tilde{\mathbf{u}}^{n+1}, \nabla p^n). \tag{3.42}$$

By taking the inner product of (3.28) with $2\delta t \mathbf{u}^{n+1}$ in the L^2 space and using (3.32), we derive

$$\frac{3\tau}{2}(\|\tilde{\mathbf{u}}^{n+1}\|^2 - \|\mathbf{u}^{n+1}\|^2) = \frac{3\tau}{2}\|\mathbf{u}^{n+1} - \tilde{\mathbf{u}}^{n+1}\|^2. \tag{3.43}$$

We combine (3.37), (3.39), (3.42), and (3.43) to obtain

$$\frac{\tau}{2}(\|\mathbf{u}^{n+1}\|^{2} - \|\mathbf{u}^{n}\|^{2} + \|2\mathbf{u}^{n+1} - \mathbf{u}^{n}\|^{2} - \|2\mathbf{u}^{n} - \mathbf{u}^{n-1}\|^{2} + \|\mathbf{u}^{n+1} - 2\mathbf{u}^{n} + \mathbf{u}^{n-1}\|^{2})
+ \frac{3\tau}{2}\|\mathbf{u}^{n+1} - \tilde{\mathbf{u}}^{n+1}\|^{2} + \frac{2\delta t^{2}}{3\tau}(\|\nabla p^{n+1}\|^{2} - \|\nabla p^{n}\|^{2}) + 2\beta\delta t\|\sqrt{\nu(\hat{\phi}^{*})}\tilde{\mathbf{u}}^{n+1}\|^{2}
= 2\delta t Q^{n+1}(\boldsymbol{\omega}^{*}\nabla \mathbf{d}^{*}, \tilde{\mathbf{u}}^{n+1}) - 2\delta t Q^{n+1}(\phi^{*}\nabla \mu^{*}, \tilde{\mathbf{u}}^{n+1})
- \frac{1-s}{2}2\delta t Q^{n+1}(\nabla \cdot (\mathbf{d}^{*}\boldsymbol{\omega}^{*}), \tilde{\mathbf{u}}^{n+1}) + \frac{1+s}{2}2\delta t Q^{n+1}(\nabla \cdot (\boldsymbol{\omega}^{*}\mathbf{d}^{*}), \tilde{\mathbf{u}}^{n+1}).$$
(3.44)

Computing the inner product of (3.21) with $2\delta t \omega^{n+1}$ in the L^2 space, we have

$$(3\mathbf{d}^{n+1} - 4\mathbf{d}^{n} + \mathbf{d}^{n-1}, \boldsymbol{\omega}^{n+1}) = -2\delta t M_{1} \|\boldsymbol{\omega}^{n+1}\|^{2} - 2\delta t Q^{n+1} (\mathbf{u}^{*} \cdot \nabla \mathbf{d}^{*}, \boldsymbol{\omega}^{n+1}) - \frac{1-s}{2} 2\delta t Q^{n+1} (\mathbf{d}^{*} \nabla \mathbf{u}^{*}, \boldsymbol{\omega}^{n+1}) + \frac{1+s}{2} 2\delta t Q^{n+1} (\mathbf{d}^{*} \cdot \nabla \mathbf{u}^{*}, \boldsymbol{\omega}^{n+1}).$$

$$(3.45)$$

Computing the L^2 inner product of (3.22) with $-(3\mathbf{d}^{n+1}-4\mathbf{d}^n+\mathbf{d}^{n-1})$, we find

$$-(\boldsymbol{\omega}^{n+1}, 3\mathbf{d}^{n+1} - 4\mathbf{d}^{n} + \mathbf{d}^{n-1}) + K(\nabla \mathbf{d}^{n+1}, \nabla (3\mathbf{d}^{n+1} - 4\mathbf{d}^{n} + \mathbf{d}^{n-1}))$$

$$+ U^{n+1}(\mathbf{H}^{*}, 3\mathbf{d}^{n+1} - 4\mathbf{d}^{n} + \mathbf{d}^{n-1})$$

$$+ C(\mathbf{d}^{n+1} - \mathbf{d}^{*}, 3\mathbf{d}^{n+1} - 4\mathbf{d}^{n} + \mathbf{d}^{n-1}) = 0.$$
(3.46)

Computing the inner product of (3.23) with $2\delta t \mu^{n+1}$ in the L^2 space, we have

$$(3\phi^{n+1} - 4\phi^n + \phi^{n-1}, \mu^{n+1}) = -2\delta t M_2 \|\nabla \mu^{n+1}\|^2 - 2\delta t Q^{n+1} (\nabla \cdot (\mathbf{u}^*\phi^*), \mu^{n+1}). \tag{3.47}$$

Computing the L^2 inner product of (3.24) with $-(3\phi^{n+1}-4\phi^n+\phi^{n-1})$, we find

$$\begin{split} -(\mu^{n+1},3\phi^{n+1}-4\phi^n+\phi^{n-1}) &+ \lambda(\nabla\phi^{n+1},\nabla(3\phi^{n+1}-4\phi^n+\phi^{n-1})) \\ &+ U^{n+1}(R^*,3\phi^{n+1}-4\phi^n+\phi^{n-1})d\mathbf{x} \\ &+ \frac{S_1}{\epsilon^2}(\phi^{n+1}-\phi^*,3\phi^{n+1}-4\phi^n+\phi^{n-1}) \\ &+ S_2(\nabla(\phi^{n+1}-\phi^*),\nabla(3\phi^{n+1}-4\phi^n+\phi^{n-1})) = 0. \end{split} \tag{3.48}$$

By multiplying (3.25) with $2U^{n+1}$ and using (3.33), we obtain

$$|U^{n+1}|^2 - |U^n|^2 + |2U^{n+1} - U^n|^2 - |2U^n - U^{n-1}|^2 + |U^{n+1} - 2U^n + U^{n-1}|^2$$

$$= U^{n+1}(\mathbf{H}^*, 3\mathbf{d}^{n+1} - 4\mathbf{d}^n + \mathbf{d}^{n-1}) + U^{n+1}(R^*, 3\phi^{n+1} - 4\phi^n + \phi^{n-1}).$$
(3.49)

By multiplying (3.27) with $2\delta t Q^{n+1}$ and use (3.33) to obtain

$$\frac{1}{2} \Big(|Q^{n+1}|^2 - |Q^n|^2 + |2Q^{n+1} - Q^n|^2 - |2Q^n - Q^{n-1}|^2 + |Q^{n+1} - 2Q^n + Q^{n-1}|^2 \Big) \\
= 2\delta t Q^{n+1} (\mathbf{u}^* \cdot \nabla \mathbf{d}^*, \boldsymbol{\omega}^{n+1}) - 2\delta t Q^{n+1} (\boldsymbol{\omega}^* \nabla \mathbf{d}^*, \tilde{\mathbf{u}}^{n+1}) \\
+ 2\delta t Q^{n+1} (\nabla \cdot (\mathbf{u}^* \boldsymbol{\phi}^*), \boldsymbol{\mu}^{n+1}) + 2\delta t Q^{n+1} (\boldsymbol{\phi}^* \nabla \boldsymbol{\mu}^*, \tilde{\mathbf{u}}^{n+1}) \\
+ \frac{1-s}{2} 2\delta t Q^{n+1} (\mathbf{d}^* \nabla \mathbf{u}^*, \boldsymbol{\omega}^{n+1}) + \frac{1-s}{2} 2\delta t Q^{n+1} (\nabla \cdot (\mathbf{d}^* \boldsymbol{\omega}^*), \tilde{\mathbf{u}}^{n+1}) \\
- \frac{1+s}{2} 2\delta t Q^{n+1} (\mathbf{d}^* \cdot \nabla \mathbf{u}^*, \boldsymbol{\omega}^{n+1}) - \frac{1+s}{2} 2\delta t Q^{n+1} (\nabla \cdot (\boldsymbol{\omega}^* \mathbf{d}^*), \tilde{\mathbf{u}}^{n+1}).$$
(3.50)

Hence, by combining (3.44)-(3.50) and using (3.33)-(3.34), we arrive at

$$\begin{split} &\frac{\tau}{2}(\|\mathbf{u}^{n+1}\|^2 - \|\mathbf{u}^n\|^2 + \|2\mathbf{u}^{n+1} - \mathbf{u}^n\|^2 - \|2\mathbf{u}^n - \mathbf{u}^{n-1}\|^2) + \frac{2\delta t^2}{3\tau}(\|\nabla p^{n+1}\|^2 - \|\nabla p^n\|^2) \\ &\quad + \frac{K}{2}(\|\nabla \mathbf{d}^{n+1}\|^2 - \|\nabla \mathbf{d}^n\|^2 + \|\nabla(2\mathbf{d}^{n+1} - \mathbf{d}^n)\|^2 - \|\nabla(2\mathbf{d}^n - \mathbf{d}^{n-1})\|^2) \\ &\quad + \frac{\lambda}{2}(\|\nabla \phi^{n+1}\|^2 - \|\nabla \phi^n\|^2 + \|\nabla(2\phi^{n+1} - \phi^n)\|^2 - \|\nabla(2\phi^n - \phi^{n-1})\|^2) \\ &\quad + (\|U^{n+1}\|^2 - \|U^n\|^2 + \|2U^{n+1} - U^n\|^2 - \|2U^n - U^{n-1}\|^2) \\ &\quad + \frac{1}{2}(\|Q^{n+1}\|^2 - \|Q^n\|^2 + \|2Q^{n+1} - Q^n\|^2 - \|2Q^n - Q^{n-1}\|^2) \\ &\quad + C(\|\mathbf{d}^{n+1} - \mathbf{d}^n\|^2 - \|\mathbf{d}^n - \mathbf{d}^{n-1}\|^2) + \frac{S_1}{\epsilon^2}(\|\phi^{n+1} - \phi^n\|^2 - \|\phi^n - \phi^{n-1}\|^2) \\ &\quad + S_2(\|\nabla(\phi^{n+1} - \phi^n)\|^2 - \|\nabla(\phi^n - \phi^{n-1})\|^2) \\ &\quad + \left\{\frac{\tau}{2}\|\mathbf{u}^{n+1} - 2\mathbf{u}^n + \mathbf{u}^{n-1}\|^2 + \frac{3\tau}{2}\|\mathbf{u}^{n+1} - \tilde{\mathbf{u}}^{n+1}\|^2 \\ &\quad + \frac{\lambda}{2}\|\nabla(\phi^{n+1} - 2\phi^n + \phi^{n-1})\|^2 + \frac{2S_1}{\epsilon^2}\|\phi^{n+1} - 2\phi^n + \phi^{n-1}\|^2 \\ &\quad + 2S_2\|\nabla(\phi^{n+1} - 2\phi^n + \phi^{n-1})\|^2 + 2C\|\mathbf{d}^{n+1} - 2\mathbf{d}^n + \mathbf{d}^{n-1}\|^2 \\ &\quad + \|U^{n+1} - 2U^n + U^{n-1}\|^2 + \frac{1}{2}|Q^{n+1} - 2Q^n + Q^{n-1}|^2 \right\} \\ &= -2\delta t\beta\|\sqrt{\nu(\hat{\phi}^*)}\tilde{\mathbf{u}}^{n+1}\|^2 - 2\delta tM_1\|\boldsymbol{\omega}^{n+1}\|^2 - 2\delta tM_2\|\nabla\mu^{n+1}\|^2. \end{split}$$

Finally, we obtain (3.35) after dropping the positive terms in $\{\}$ from (3.51).

3.3. Decoupled implementation using the nonlocal splitting method

In this subsection, we develop the decoupling implementation process for the scheme (3.21)-(3.28). Using the nonlocal attribute of the auxiliary variable Q, we split all variables into multiple variables and then merge them back

Step 1: we split \mathbf{d}^{n+1} , $\boldsymbol{\omega}^{n+1}$, $\boldsymbol{\phi}^{n+1}$, $\boldsymbol{\mu}^{n+1}$, \boldsymbol{U}^{n+1} into a linear combination form in terms of Q^{n+1} , namely,

$$\begin{cases} \mathbf{d}^{n+1} = \mathbf{d}_{1}^{n+1} + Q^{n+1} \mathbf{d}_{2}^{n+1}, \, \boldsymbol{\omega}^{n+1} = \boldsymbol{\omega}_{1}^{n+1} + Q^{n+1} \boldsymbol{\omega}_{2}^{n+1}, \\ \phi^{n+1} = \phi_{1}^{n+1} + Q^{n+1} \phi_{2}^{n+1}, \, \mu^{n+1} = \mu_{1}^{n+1} + Q^{n+1} \mu_{2}^{n+1}, \\ U^{n+1} = U_{1}^{n+1} + Q^{n+1} U_{2}^{n+1}. \end{cases}$$
(3.52)

We solve $\mathbf{d}_i^{n+1}, \boldsymbol{\omega}_i^{n+1}, \phi_i^{n+1}, \mu_i^{n+1}$ for i=1,2, as follows. Using (3.52), we replace $\mathbf{d}^{n+1}, \boldsymbol{\omega}^{n+1}, \phi^{n+1}, \mu^{n+1}, \mu^{n+1}, \mu^{n+1}$ in the system (3.21)-(3.24), and decompose the obtained equations according to Q^{n+1} into the following four subsystems:

$$\begin{cases}
\frac{a}{2M_{1}\delta t}\mathbf{d}_{1}^{n+1} = -\boldsymbol{\omega}_{1}^{n+1} + \frac{b\mathbf{d}^{n} - c\mathbf{d}^{n-1}}{2M_{1}\delta t}, \\
\boldsymbol{\omega}_{1}^{n+1} = -K\Delta\mathbf{d}_{1}^{n+1} + \mathbf{H}^{*}U_{1}^{n+1} + C(\mathbf{d}_{1}^{n+1} - \mathbf{d}^{*}),
\end{cases} (3.53)$$

$$\begin{cases} \frac{a}{2M_1\delta t}\mathbf{d}_2^{n+1} = -\boldsymbol{\omega}_2^{n+1} - \frac{1}{M_1}\mathbf{u}^* \cdot \nabla \mathbf{d}^* - \frac{1}{M_1}\frac{1-s}{2}\mathbf{d}^*\nabla \mathbf{u}^* + \frac{1}{M_1}\frac{1+s}{2}\mathbf{d}^* \cdot \nabla \mathbf{u}^*, \\ \boldsymbol{\omega}_2^{n+1} = -K\Delta \mathbf{d}_2^{n+1} + \mathbf{H}^* \boldsymbol{U}_2^{n+1} + C\mathbf{d}_2^{n+1}, \end{cases}$$
(3.54)

$$\begin{cases} \frac{a}{2M_{2}\delta t}\phi_{1}^{n+1} = \Delta\mu_{1}^{n+1} + \frac{b\phi^{n} - c\phi^{n-1}}{2M_{2}\delta t}, \\ \mu_{1}^{n+1} = -\lambda\Delta\phi_{1}^{n+1} + R^{*}U_{1}^{n+1} + \frac{S_{1}}{\epsilon^{2}}(\phi_{1}^{n+1} - \phi^{*}) - S_{2}\Delta(\phi_{1}^{n+1} - \phi^{*}), \end{cases}$$
(3.55)

$$\begin{cases} \frac{a}{2M_2\delta t}\phi_2^{n+1} = \Delta\mu_2^{n+1} - \frac{1}{M_2}\nabla\cdot(\phi^*\mathbf{u}^*), \\ \mu_2^{n+1} = -\lambda\Delta\phi_2^{n+1} + R^*U_2^{n+1} + \frac{S_1}{\epsilon^2}\phi_2^{n+1} - S_2\Delta\phi_2^{n+1}. \end{cases}$$
(3.56)

We continue to split \mathbf{d}_i^{n+1} , $\boldsymbol{\omega}_i^{n+1}$, $\boldsymbol{\phi}_i^{n+1}$, $\boldsymbol{\mu}_i^{n+1}$ for i=1,2 using the nonlocal variables U_1^{n+1} and U_2^{n+1} . Namely, for i=1,2, we formulate \mathbf{d}_i^{n+1} , $\boldsymbol{\omega}_i^{n+1}$, $\boldsymbol{\phi}_i^{n+1}$, $\boldsymbol{\mu}_i^{n+1}$ as

$$\begin{cases}
\mathbf{d}_{i}^{n+1} = \mathbf{d}_{i1}^{n+1} + U_{i}^{n+1} \mathbf{d}_{i2}^{n+1}, \, \boldsymbol{\omega}_{i}^{n+1} = \boldsymbol{\omega}_{i1}^{n+1} + U_{i}^{n+1} \boldsymbol{\omega}_{i2}^{n+1}, \\
\boldsymbol{\phi}_{i}^{n+1} = \boldsymbol{\phi}_{i1}^{n+1} + U_{i}^{n+1} \boldsymbol{\phi}_{i2}^{n+1}, \, \boldsymbol{\mu}_{i}^{n+1} = \boldsymbol{\mu}_{i1}^{n+1} + U_{i}^{n+1} \boldsymbol{\mu}_{i2}^{n+1}.
\end{cases}$$
(3.57)

Using (3.57), we replace \mathbf{d}_i^{n+1} , $\boldsymbol{\omega}_i^{n+1}$, $\boldsymbol{\phi}_i^{n+1}$, $\boldsymbol{\mu}_i^{n+1}$ in the four subsystems (3.53)-(3.56), and decompose the obtained equations according to U_1^{n+1} and U_2^{n+1} to the following eight sub-systems:

$$\begin{cases} \frac{a}{2M_1\delta t}\mathbf{d}_{i1}^{n+1} = -\boldsymbol{\omega}_{i1}^{n+1} + G_{i1}, \\ \boldsymbol{\omega}_{i}^{n+1} = -K\Delta\mathbf{d}_{i1}^{n+1} + C\mathbf{d}_{i1}^{n+1} + L_{i1}, i = 1, 2. \end{cases}$$
(3.58)

$$\begin{cases} \frac{a}{2M_1\delta t}\mathbf{d}_{i2}^{n+1} = -\boldsymbol{\omega}_{i2}^{n+1}, \\ \boldsymbol{\omega}_{i2}^{n+1} = -K\Delta\mathbf{d}_{i2}^{n+1} + \mathbf{H}^* + C\mathbf{d}_{i2}^{n+1}, i = 1, 2, \end{cases}$$
(3.59)

$$\begin{cases}
\frac{a}{2M_{1}\delta t}\mathbf{d}_{i1}^{n+1} = -\boldsymbol{\omega}_{i1}^{n+1} + G_{i1}, \\
\boldsymbol{\omega}_{i1}^{n+1} = -K\Delta \mathbf{d}_{i1}^{n+1} + C\mathbf{d}_{i1}^{n+1} + L_{i1}, i = 1, 2, \\
\begin{cases}
\frac{a}{2M_{1}\delta t}\mathbf{d}_{i2}^{n+1} = -\boldsymbol{\omega}_{i2}^{n+1}, \\
\boldsymbol{\omega}_{i2}^{n+1} = -K\Delta \mathbf{d}_{i2}^{n+1} + \mathbf{H}^* + C\mathbf{d}_{i2}^{n+1}, i = 1, 2, \\
\end{cases} \\
\begin{cases}
\frac{a}{2M_{2}\delta t}\boldsymbol{\phi}_{i1}^{n+1} = \Delta \mu_{i1}^{n+1} + \hat{G}_{i1}, \\
\boldsymbol{\mu}_{i1}^{n+1} = -\lambda \Delta \boldsymbol{\phi}_{i1}^{n+1} + \frac{S_{1}}{\epsilon^{2}}\boldsymbol{\phi}_{i1}^{n+1} - S_{2}\Delta \boldsymbol{\phi}_{i1}^{n+1} + \hat{L}_{i1}, i = 1, 2, \\
\end{cases} \tag{3.58}$$

$$\begin{cases} \frac{a}{2M_2\delta t}\phi_{i2}^{n+1} = \Delta\mu_{i2}^{n+1}, \\ \mu_{i2}^{n+1} = -\lambda\Delta\phi_{i2}^{n+1} + R^* + \frac{S_1}{\epsilon^2}\phi_{i2}^{n+1} - S_2\Delta\phi_{i2}^{n+1}, i = 1, 2, \end{cases}$$
(3.61)

where

$$\begin{cases} G_{11} = \frac{b\mathbf{d}^{n} - c\mathbf{d}^{n-1}}{2M_{1}\delta t}, \\ G_{21} = -\frac{1}{M_{1}}\mathbf{u}^{*} \cdot \nabla \mathbf{d}^{*} - \frac{1}{M_{1}}\frac{1-s}{2}\mathbf{d}^{*}\nabla \mathbf{u}^{*} + \frac{1}{M_{1}}\frac{1+s}{2}\mathbf{d}^{*} \cdot \nabla \mathbf{u}^{*}, \\ L_{11} = -C\mathbf{d}^{*}, L_{21} = 0, \\ \hat{G}_{11} = \frac{b\phi^{n} - c\phi^{n-1}}{2M_{2}\delta t}, \hat{G}_{21} = -\frac{1}{M_{2}}\nabla \cdot (\mathbf{u}^{*}\phi^{*}), \\ \hat{L}_{11} = -\frac{S_{1}}{\epsilon^{2}}\phi^{*} + S_{2}\Delta\phi^{*}, \hat{L}_{21} = 0. \end{cases}$$

It is very easy to solve (3.58)-(3.61) since all equations in these systems are linear and elliptic with constant coefficients. Meanwhile, note that the equation of \mathbf{d}_{12}^{n+1} , $\boldsymbol{\omega}_{12}^{n+1}$ is the same as that of \mathbf{d}_{22}^{n+1} , $\boldsymbol{\omega}_{22}^{n+1}$, the equation of $\boldsymbol{\phi}_{12}^{n+1}$, $\boldsymbol{\mu}_{12}^{n+1}$ is the same as that of $\boldsymbol{\phi}_{22}^{n+1}$, $\boldsymbol{\mu}_{22}^{n+1}$, thus we only need to solve six elliptic systems here.

Step 2: we further solve U_1^{n+1} and U_2^{n+1} . We rewrite (3.25) to be the following form:

$$U^{n+1} = \frac{1}{2} (\mathbf{H}^*, \mathbf{d}^{n+1}) + \frac{1}{2} (R^*, \phi^{n+1}) + g^n, \tag{3.62}$$

where $g^n = \frac{1}{3}(bU^n - cU^{n-1}) - \frac{1}{6}(\mathbf{H}^*, b\mathbf{d}^n - c\mathbf{d}^{n-1}) - \frac{1}{6}(R^*, b\phi^n - c\phi^{n-1})$, and replace $U^{n+1}, \mathbf{d}^{n+1}, \phi^{n+1}$ using (3.52) to get

$$U_1^{n+1} + Q^{n+1}U_2^{n+1} = \frac{1}{2}(\mathbf{H}^*, \mathbf{d}_1^{n+1} + Q^{n+1}\mathbf{d}_2^{n+1}) + \frac{1}{2}(R^*, \phi_1^{n+1} + Q^{n+1}\phi_2^{n+1}) + g^n.$$
(3.63)

According to Q^{n+1} , we split (3.63) into the following two equalities:

$$U_i^{n+1} = \frac{1}{2} (\mathbf{H}^*, \mathbf{d}_i^{n+1}) + \frac{1}{2} (R^*, \phi_i^{n+1}) d\mathbf{x} + G_U^i, i = 1, 2,$$
(3.64)

where $G_U^1 = g^n$, $G_U^2 = 0$. We continue to replace \mathbf{d}_i^{n+1} , ϕ_i^{n+1} with i = 1, 2 in (3.64) using (3.57) and apply a simple factor-

$$U_i^{n+1} = \frac{\frac{1}{2}(\mathbf{H}^*, \mathbf{d}_{i1}^{n+1}) + \frac{1}{2}(R^*, \phi_{i1}^{n+1}) + G_U^i}{1 - \frac{1}{2}(\mathbf{H}^*, \mathbf{d}_{i2}^{n+1}) - \frac{1}{2}(R^*, \phi_{i2}^{n+1})}, i = 1, 2.$$
(3.65)

Thus one can directly solve U_1^{n+1} , U_2^{n+1} from (3.65) under of the premise that the denominators are non-zero (shown

We show the solvability of (3.65) as follows. For the system of (3.59), by taking the L^2 inner product of the first equation with $-\omega_{i2}^{n+1}$, of the second equation with $\frac{a}{2M_1\delta t}\mathbf{d}_{i2}^{n+1}$, and combine the obtained two equations, we deduce

$$-\frac{a}{2M_1\delta t}(\mathbf{H}^*, \mathbf{d}_{i2}^{n+1}) = \|\boldsymbol{\omega}_{i2}^{n+1}\|^2 + \frac{aK}{2M_1\delta t}\|\nabla \mathbf{d}_{i2}^{n+1}\|^2 + \frac{aC}{2M_1\delta t}\|\mathbf{d}_{i2}^{n+1}\|^2 \ge 0, i = 1, 2.$$
(3.66)

In the similar way, by taking the L^2 inner product of the first equation in (3.61) with $-\mu_{i2}^{n+1}$, of the second equation with $\frac{a}{2M_2\delta t}\phi_{i2}^{n+1}$, and combine the obtained two equalities, we get

$$-\frac{a}{2M_{2}\delta t}(R^{*},\phi_{i2}^{n+1}) = \|\nabla\mu_{i2}^{n+1}\|^{2} + \frac{a\lambda}{2M_{2}\delta t}\|\nabla\phi_{i2}^{n+1}\|^{2} + \frac{aS_{1}}{2M_{2}\epsilon^{2}\delta t}\|\phi_{i2}^{n+1}\|^{2} + \frac{aS_{2}}{2M_{2}\delta t}\|\nabla\phi_{i2}^{n+1}\|^{2} \ge 0, i = 1, 2.$$

$$(3.67)$$

Hence, the denominators in (3.65) for i=1,2 are always non-zero, which means (3.65) is always solvable. After U_1^{n+1}, U_2^{n+1} are obtained using (3.65), $\mathbf{d}_i^{n+1}, \boldsymbol{\omega}_i^{n+1}, \boldsymbol{\mu}_i^{n+1}$ with i=1,2 can be updated from (3.57) directly.

Step 3: we solve the velocity field $\tilde{\mathbf{u}}^{n+1}$ in (3.26). We formulate $\tilde{\mathbf{u}}^{n+1}$ to be the split form as

$$\tilde{\mathbf{u}}^{n+1} = \tilde{\mathbf{u}}_1^{n+1} + Q^{n+1} \tilde{\mathbf{u}}_2^{n+1}. \tag{3.68}$$

After replacing the variable $\tilde{\mathbf{u}}^{n+1}$ in (3.26) with (3.68), and splitting the obtained equations in terms of Q^{n+1} , we can obtain two sub-systems:

$$\left(\frac{a\tau}{2\delta t} + \beta v(\hat{\phi}^*)\right) \tilde{\mathbf{u}}_i^{n+1} = R_{\mathbf{u}}^i, i = 1, 2, \tag{3.69}$$

where

$$\begin{cases}
R_{\mathbf{u}}^{1} = -\nabla p^{n} + \tau \frac{b\mathbf{u}^{n} - c\mathbf{u}^{n-1}}{2\delta t}, \\
R_{\mathbf{u}}^{2} = -\phi^{*}\nabla \mu^{*} + \boldsymbol{\omega}^{*}\nabla \mathbf{d}^{*} - \frac{1-s}{2}\nabla \cdot (\mathbf{d}^{*}\boldsymbol{\omega}^{*}) + \frac{1+s}{2}\nabla \cdot (\boldsymbol{\omega}^{*}\mathbf{d}^{*}).
\end{cases} (3.70)$$

It is very easy to solve (3.69) since they are just linear algebraic equations. Moreover, since $\nu(\hat{\phi}^*) \ge \min(\nu_1, \nu_2) > 0$, we have $\frac{a\tau}{2\delta t} + \beta\nu(\hat{\phi}^*) > 0$ which shows (3.69) is always solvable.

Step 4: we solve Q^{n+1} in (3.27). By using the linear combination forms for the variables ω^{n+1} , μ^{n+1} in (3.52), $\tilde{\mathbf{u}}^{n+1}$ in (3.68), we formulate (3.27) into the following form:

$$\left(\frac{3}{2\delta t} - \eta_2\right) Q^{n+1} = \frac{1}{2\delta t} (4Q^n - Q^{n-1}) + \eta_1, \tag{3.71}$$

where n_i is given as

$$\eta_{i} = (\mathbf{u}^{*} \cdot \nabla \mathbf{d}^{*}, \boldsymbol{\omega}_{i}^{n+1}) - (\boldsymbol{\omega}^{*} \nabla \mathbf{d}^{*}, \tilde{\mathbf{u}}_{i}^{n+1}) + (\nabla \cdot (\boldsymbol{\phi}^{*} \mathbf{u}^{*}), \boldsymbol{\mu}_{i}^{n+1}) + (\boldsymbol{\phi}^{*} \nabla \boldsymbol{\mu}^{*}, \tilde{\mathbf{u}}_{i}^{n+1}) \\
+ \frac{1 - s}{2} (\mathbf{d}^{*} \nabla \mathbf{u}^{*}, \boldsymbol{\omega}_{i}^{n+1}) + \frac{1 - s}{2} (\nabla \cdot (\mathbf{d}^{*} \boldsymbol{\omega}^{*}), \tilde{\mathbf{u}}_{i}^{n+1}) \\
- \frac{1 + s}{2} (\mathbf{d}^{*} \cdot \nabla \mathbf{u}^{*}, \boldsymbol{\omega}_{i}^{n+1}) - \frac{1 + s}{2} (\nabla \cdot (\boldsymbol{\omega}^{*} \mathbf{d}^{*}), \tilde{\mathbf{u}}_{i}^{n+1}), i = 1, 2. \tag{3.72}$$

It is very easy to solve (3.71) since all terms contained in η_1 and η_2 are already obtained from Step 1-Step 3 (solvability of (3.71) is given below). Once Q^{n+1} is obtained from (3.71), we update $\tilde{\mathbf{u}}^{n+1}$ from (3.68), and \mathbf{d}^{n+1} , $\boldsymbol{\omega}^{n+1}$, ϕ^{n+1} , μ^{n+1} , U^{n+1} from (3.52).

We further show the solvability of (3.71) by proving $\frac{3}{2\delta t} - \eta_2 \neq 0$. By taking the L^2 inner product of (3.69) for i = 2 with $\tilde{\mathbf{u}}_2^{n+1}$, we deduce

$$-(\phi^* \nabla \mu^*, \tilde{\mathbf{u}}_2^{n+1}) + (\boldsymbol{\omega}^* \nabla \mathbf{d}^*, \tilde{\mathbf{u}}_2^{n+1}) - \frac{1-s}{2} (\nabla \cdot (\mathbf{d}^* \boldsymbol{\omega}^*), \tilde{\mathbf{u}}_2^{n+1}) + \frac{1+s}{2} (\nabla \cdot (\boldsymbol{\omega}^* \mathbf{d}^*), \tilde{\mathbf{u}}_2^{n+1})$$

$$= \frac{a\tau}{2\delta t} \|\tilde{\mathbf{u}}_2^{n+1}\|^2 + \beta \|\sqrt{\nu(\hat{\phi}^*)} \tilde{\mathbf{u}}_2^{n+1}\|^2 \ge 0.$$
(3.73)

By taking the L^2 inner product of the first equation in (3.54) with $M_1\omega_2^{n+1}$, of the second equation in (3.54) with $-\frac{a}{2\delta t}\mathbf{d}_2^{n+1}$, of the first equation in (3.56) with $M_2\mu_2^{n+1}$, of the second equation in (3.56) with $-\frac{a}{2\delta t}\phi_2^{n+1}$, and combining the four obtained equations, we get

$$- (\mathbf{u}^* \cdot \nabla \mathbf{d}^*, \boldsymbol{\omega}_2^{n+1}) - (\nabla \cdot (\boldsymbol{\phi}^* \mathbf{u}^*), \boldsymbol{\mu}_2^{n+1}) - \frac{1-s}{2} (\mathbf{d}^* \nabla \mathbf{u}^*, \boldsymbol{\omega}_2^{n+1}) + \frac{1+s}{2} (\mathbf{d}^* \cdot \nabla \mathbf{u}^*, \boldsymbol{\omega}_2^{n+1})$$

$$= M_1 \|\boldsymbol{\omega}_2^{n+1}\|^2 + \frac{aK}{2\delta t} \|\nabla \mathbf{d}_2^{n+1}\|^2 + \frac{aC}{2\delta t} \|\mathbf{d}_2^{n+1}\|^2$$

$$+ M_2 \|\nabla \boldsymbol{\mu}_2^{n+1}\|^2 + \frac{a\lambda}{2\delta t} \|\nabla \boldsymbol{\phi}_2^{n+1}\|^2 + \frac{aS_1}{2\delta t\epsilon^2} \|\boldsymbol{\phi}_2^{n+1}\|^2 + \frac{aS_2}{2\delta t} \|\nabla \boldsymbol{\phi}_2^{n+1}\|^2$$

$$+ \frac{a}{2\delta t} U_2^{n+1} \left((\mathbf{H}^*, \mathbf{d}_2^{n+1}) + (R^*, \boldsymbol{\phi}_2^{n+1}) \right).$$

$$(3.74)$$

From (3.64) with i = 2, we get

$$U_2^{n+1}\left((\mathbf{H}^*,\mathbf{d}_2^{n+1})+(R^*,\phi_2^{n+1})\right)=2(U_2^{n+1})^2\geq 0. \tag{3.75}$$

From (3.73), (3.74) and (3.75), we get $-\eta_2 \ge 0$. Thus (3.71) is always solvable.

Step 5: we update \mathbf{u}^{n+1} and p^{n+1} from (3.28) and (3.29).

As can be seen from the above detailed implementation process, the calculation of all unknown variables has been completely decoupled, and all nonlinear terms will not bring any unnecessary iterations. At each time step, the total computational cost is just to solve several independent elliptic equations. The decoupling of all equations and the characteristic of having only constant coefficients means very efficient practical calculations.

Remark 3.6. For the sake of completeness, here we present the fully-decoupled scheme developed in [34,35] for solving the Darcy coupled Cahn-Hilliard equation. For simplicity, only the first-order time accurate scheme is given here, since the second-order version follows the same line of algorithm design. To see the scheme more accurately, we only discretize related terms, while other irrelevant terms remain unchanged. The scheme developed in [34,35] reads as

$$\phi_t + \underbrace{\nabla \cdot (\mathbf{u}^{n+1}\phi^n)}_{\text{translition anglish}} = M\Delta\mu^{n+1},\tag{3.76}$$

$$\tau \frac{\mathbf{u}^{n+1} - \mathbf{u}^n}{\delta t} + \beta \nu(\phi) \mathbf{u}^{n+1} + \nabla p^n + \underbrace{\phi^n \nabla \mu^{n+1}}_{\text{Implicit-explicit}} = 0.$$
(3.77)

Note that the advection $\nabla \cdot (\mathbf{u}\phi)$ and surface tension $\phi \nabla \mu$ are discretized using the traditional implicit-explicit combination method. Due to the special format of the Darcy equations, by using the explicit linear relationship between \mathbf{u}^{n+1} and other items, the decoupling structure of the above scheme can be obtained. More precisely, one can rewrite (3.77) as

$$\mathbf{u}^{n+1} = \frac{1}{\frac{\tau}{\epsilon_n} + \beta \nu(\phi)} \left(\frac{\tau}{\delta t} \mathbf{u}^n - \nabla p^n + \phi^n \nabla \mu^{n+1} \right). \tag{3.78}$$

Then, by replacing \mathbf{u}^{n+1} in the scheme (3.76) using (3.78), the scheme for the Cahn-Hilliard equation is formulated as

$$\phi_t + \nabla \cdot \left(\frac{1}{\frac{\tau}{\delta t} + \beta \nu(\phi)} (\frac{\tau}{\delta t} \mathbf{u}^n - \nabla p^n + \phi^n \nabla \mu^{n+1}) \phi^n \right) = M \Delta \mu^{n+1}.$$
(3.79)

In this way, the scheme (3.79) does achieve a full decoupling structure, that is, the computation of ϕ^{n+1} is independent of the velocity field \mathbf{u}^{n+1} . However, the paid price is that the equation of ϕ is then equipped with variable coefficients (i.e., the coefficients of μ^{n+1} are not constants) at each time step, which increases the practical computational cost.

Moreover, it is worth noting that if we apply similar techniques to the DNN model considered in this article, (3.78) will definitely include many terms related to \mathbf{d} , $\boldsymbol{\omega}$. This means the Cahn-Hilliard equation for $\boldsymbol{\phi}$ and the nematic equation for \mathbf{d} will be coupled together. Therefore, the decoupling technique designed in [34,35] actually cannot obtain the expected full decoupling structure for the DNN model.

4. Numerical examples

In this section, we first implement several numerical examples to verify the energy stability and convergence rate of the proposed scheme (3.21)-(3.29) (denoted by Stab for short). Then, we conduct several benchmark simulations on the Saffman-Taylor fingering instability problems to show the effectiveness of the scheme. Since the Hele-Shaw cell refers to two wide parallel plates with a small gap, most of the numerical simulations related to it are 2D (cf. [2,7,9,10,15,16,18,53,63,64]), so this article only considers 2D simulation as well. In all the examples below, the computed domain is set to a rectangular shape, and the spectral Legendre-Galerkin method is used for spatial discretization.

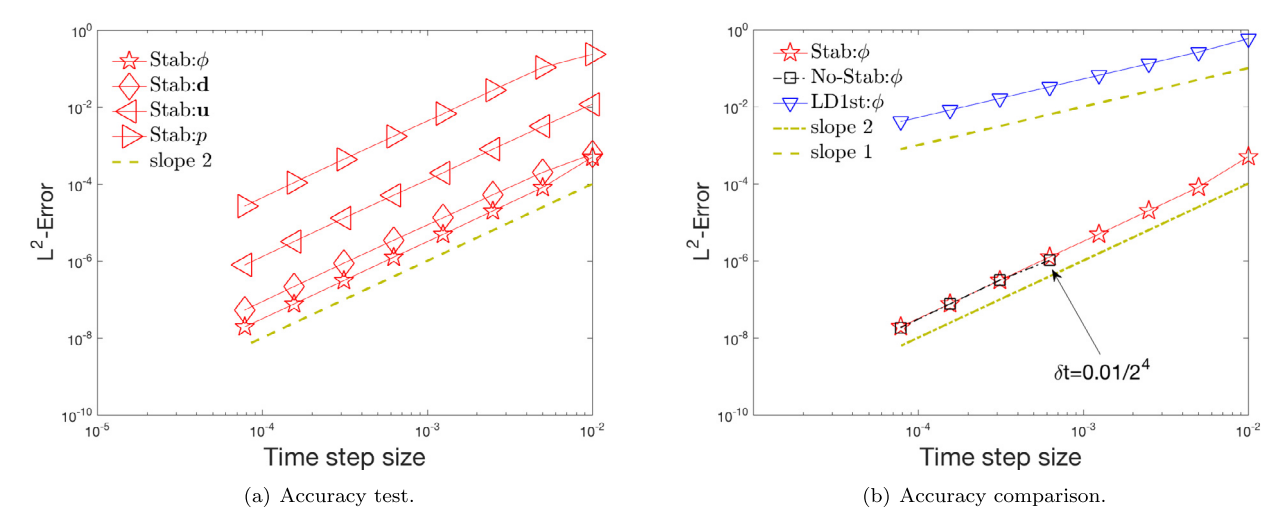


Fig. 4.1. (a) The numerical errors in L^2 for all variables that are computed using the schemes Stab with various time steps; (b) the numerical errors in L^2 for ϕ that are computed using the schemes Stab/No-Stab/LD1st with various time steps; (note: those error points of No-Stab for time steps $\delta t > 0.01/2^4$ are omitted since No-Stab blows up quickly).

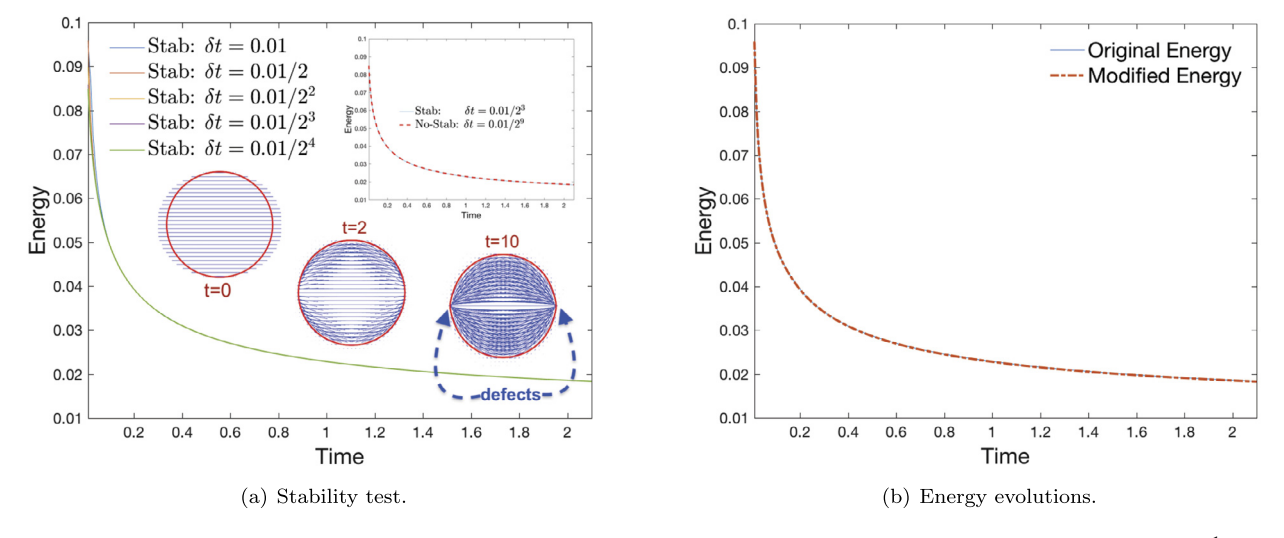


Fig. 4.2. (a) Evolution of the total free energy (3.36) over time that is calculated by Stab and No-Stab with different time steps (profiles of $\{\phi = \frac{1}{2}\}$ and director field **d** at t = 0, 2, 10 are appended); (b) the comparisons of the original energy (2.15) and the modified energy (3.36) computed by using the time step $\delta t = 0.01$.

4.1. Tests of accuracy and stability

We perform refinement tests on the time step size to verify the convergence order of the proposed scheme (3.21)-(3.29). Moreover, we will compare the developed scheme with other version of numerical schemes on the accuracy/stability/efficiency, including the non-stabilized version (the same scheme (3.21)-(3.29) but with $C = S_1 = S_2 = 0$, referred to as No-Stab, for short), the first-order, linear and decoupled scheme developed in [60] (referred to LD1st, for short), and the nonlinear coupled scheme developed in [85] (referred to NC-scheme, for short).

We set the 2D computational domain to $\Omega = [0, 2\pi]^2$, and use the Legendre-Galerkin method to discretize the space. Each direction uses Legendre polynomials of degrees up to 256, so the error caused by spatial discretization can be ignored compared with the time discretization error. The initial conditions read as

$$\phi^0 = \frac{1}{2} \tanh\left(\frac{r_0 - |\mathbf{x} - \mathbf{x}_0|}{2\epsilon}\right) + \frac{1}{2}, \mathbf{d}^0 = (\mathbf{d}_1^0, \mathbf{d}_2^0) = (\phi^0, 0), \quad \mathbf{u}^0 = (0, 0), p^0 = 0, \tag{4.1}$$

with $r_0 = 1.3$, $\mathbf{x}_0 = (x_0, y_0) = (\pi, \pi)$. We set the model parameters as follows,

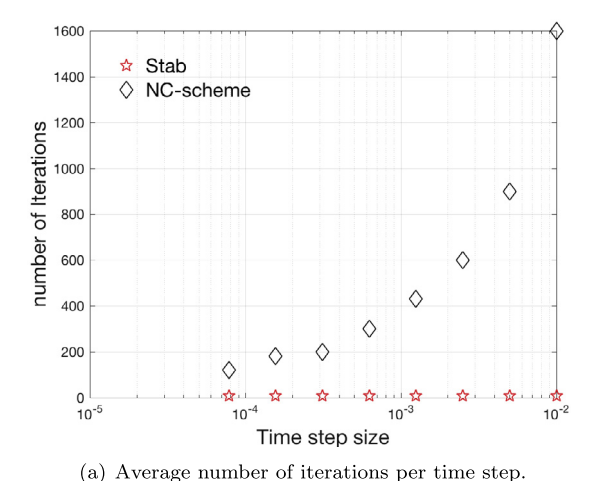


Fig. 4.3. The comparisons of the average number of iterations per time step computed by the scheme Stab and the NC-scheme developed in [85].

$$\begin{cases} M_1 = 0.01, \epsilon = 0.1, \lambda = 0.01, B = 1, s = 1.2, \phi_c = 1/2, \\ M_2 = 1, K = 0.01, \alpha = 1, \nu_1 = \nu_2 = 1, \gamma = 1, \eta = 0.01, \\ \tau = 1, \beta = 500, C = 0.02, S_1 = 4, S_2 = 0.02, \end{cases}$$

$$(4.2)$$

where the three stabilization parameters $S_1 \sim O(1)$, $C \sim O(\eta)$ and $S_2 \sim O(\eta)$ (from Remark 3.5). Since the exact solution of the system is unknown, we will deal with the numerical solution by using the very tiny time step size $\delta t = 1e - 9$ calculated by the scheme Stab as the exact solution. By changing time steps, we calculate the L^2 errors of all variables at t = 1 between the exact and the approximate solution.

In Fig. 4.1 (a), the L^2 numerical errors of all variables calculated by the scheme Stab, where we can see every variable follows the second-order temporal convergence rate. In Fig. 4.1 (b), we compare the L^2 error of the phase-field variable ϕ obtained by the scheme Stab and its non-stabilized version of No-stab, and the scheme LD1st. When the time step is greater than $0.01/2^4$, the scheme No-Stab blows up thus the corresponding error points are lost. Only for the small time step of $\delta t \leq 0.01/2^4$, the scheme No-Stab exhibits the second-order convergence rate. In contrast, the second-order time accuracy is well obtained by the scheme Stab, which means that the stability is well controlled by the stabilization terms. The LD1st scheme is always stable, but its convergence rate is first-order, and the error obtained is much rougher than the second-order scheme.

By drawing energy evolution curves with different time steps, we further show whether the scheme Stab is unconditionally energy stable. In Fig. 4.2(a), we plot the evolution curve of the total free energy (3.35), which is calculated by the scheme Stab using five different time steps. It can be seen that all the obtained energy curves show a monotonic decay trend, which shows that the scheme Stab is stable. We also use the scheme No-Stab to test this example, however, when $\delta t > 0.01/2^9$, No-stab blows up quickly. Thus, in the small inset figure of Fig. 4.2(a), we compare the energy evolution curve computed by No-Stab with $\delta t = 0.01/2^9$ and Stab with $\delta t = 0.01/2^3$. These two curves are very consistent. This means that for this particular example, to get two energy evolution curves with no obvious difference, the time step used in Stab can even be $2^6 = 64$ times larger than the time step used in No-Stab.

In Fig. 4.2(a), we also attach the profiles of the phase-field variable ϕ and director-field \mathbf{d} at different times. Due to the parallel anchoring condition ($\gamma=1$), the LC droplet slightly deforms, and the elastic energy distorts the director field to align it with the droplet interface. Two obvious defects appear on the left and right ends of the droplet interface (highlighted on the Fig. 4.2(a)). In Fig. 4.2(b), we compare the temporal evolution curve of the total free energy (2.15) (in the original form) and (3.36) (in the modified discrete form) using $\delta t=0.01$. We can see that the two energy curves are very consistent.

To demonstrate the effectiveness of the developed scheme, in Fig. 4.3, the average number of iterations per time step needed by the scheme Stab and that needed by the NC-scheme (a nonlinear coupled scheme developed in [85]) are compared. It can be seen that the efficiency of Stab is much higher than that of NC-scheme. By taking $\delta t = 0.01$ as the example, NC-scheme needs approximately 1600 iterations per time step, while Stab only requires to solve 7 elliptic equations with constant coefficients (so we count 7 iterations for the scheme Stab).

4.2. Saffman-Taylor fingering instability

In this subsection, we simulate one of the most in-depth benchmark research problems in fluid dynamic systems, the so-called Saffman-Taylor fingering pattern instability problem, which is used to demonstrate the formation and evolution of elaborate patterned structures. When a low-viscosity fluid displaces another high-viscosity fluid between the narrow-spaced plates of the Hele-Shaw cell, the interface instability will increase, resulting in a finger-like pattern. Several widely studied

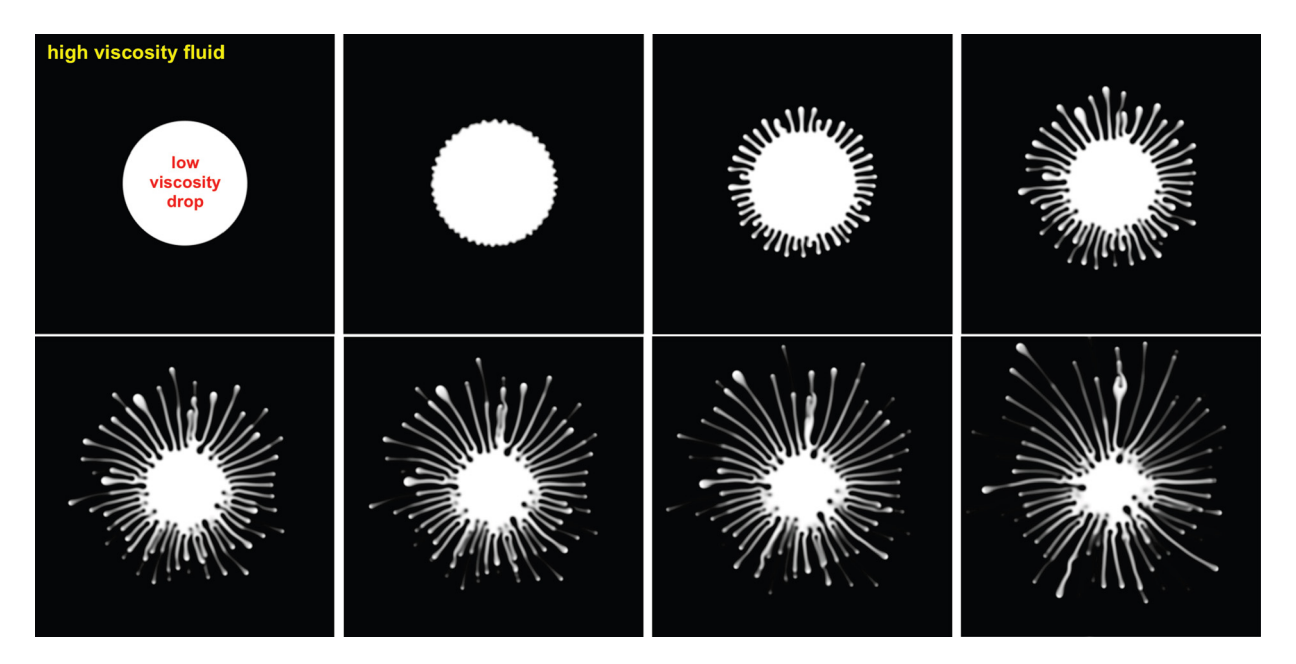


Fig. 4.4. A viscous droplet (Newtonian-Newtonian) in the rotating Hele-Shaw cell. Snapshots of the phase-field variable ϕ are taken at t = 0, 1, 1.5, 2, 3.2 (grayscale image).

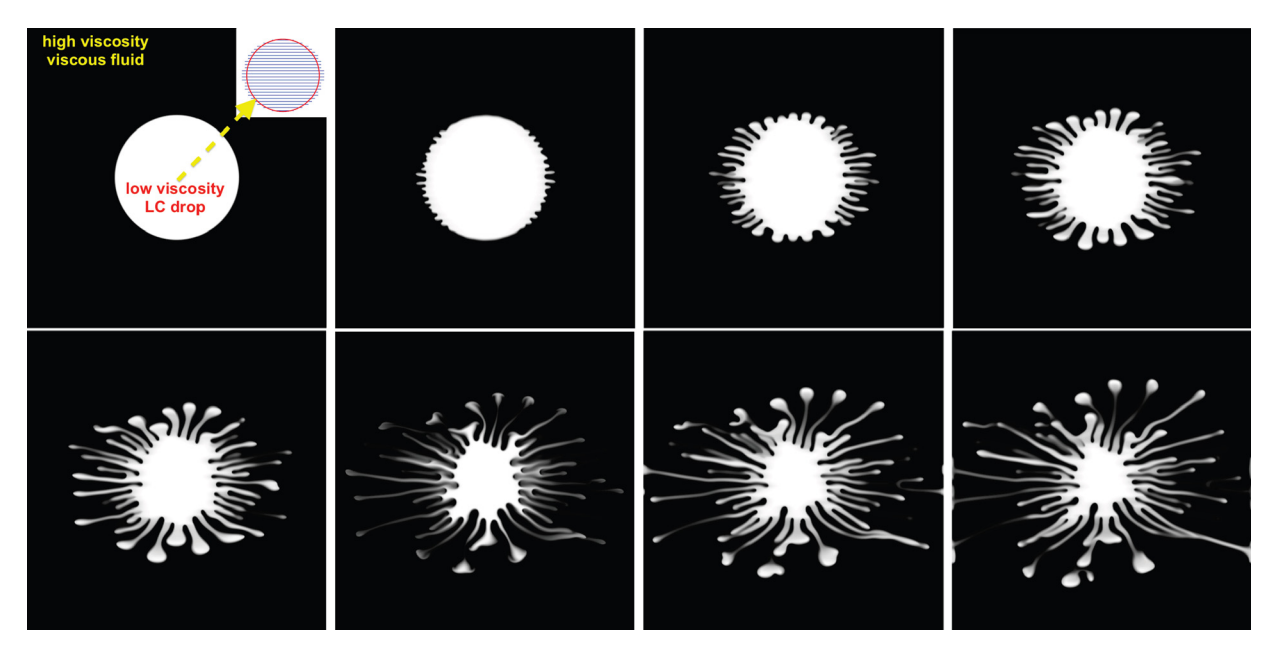
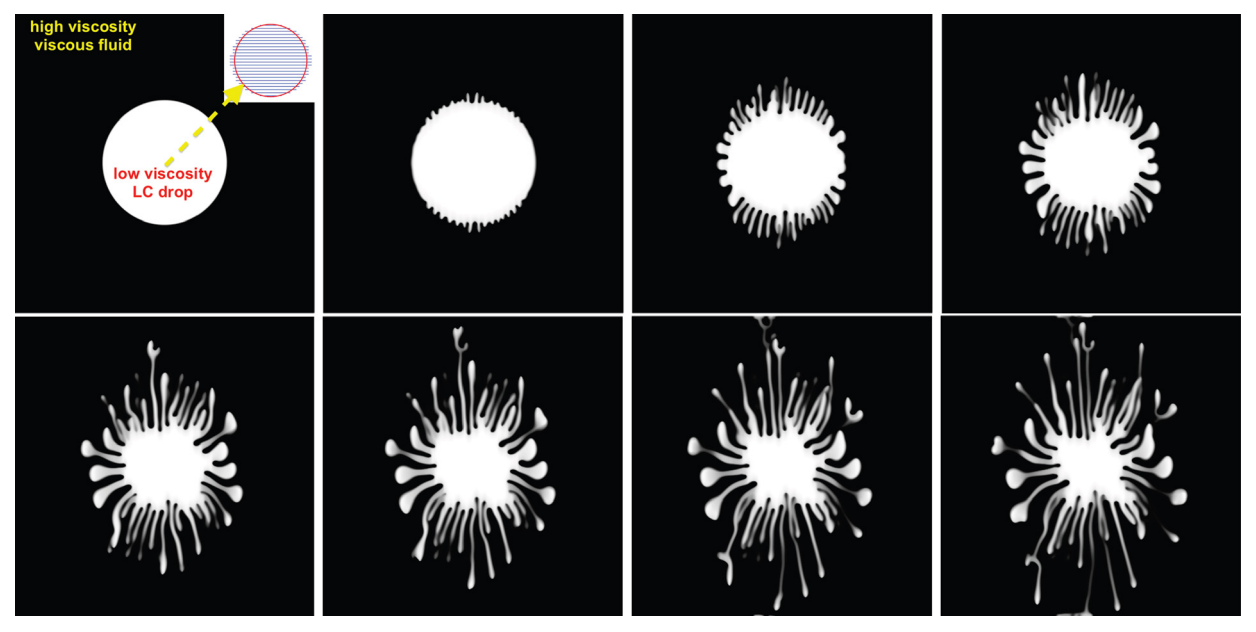


Fig. 4.5. A nematic LC droplet with parallel anchoring in the rotating Hele-Shaw cell. Snapshots of the phase-field variable ϕ in the grayscale image are plotted at t = 0, 0.5, 1, 1.5, 2, 2.5, 2.7 and 3 (\mathbf{d}^0 is appended on the first subfigure).

versions of this problem are rotating Hele-Shaw cell [2,10,53,64], or continuous radial injection [7,16,18,53]. Below we carry out numerical simulations on these two flow regimes respectively. We follow the similar procedure of nondimensionalization given in [51], and continue to use the same letters to denote the dimensionless variables and parameters, so the model (2.6)-(2.11) can be considered to be in dimensionless form. The magnitude of all dimensionless parameters adopted here is consistent with the parameters used in [51,78]. We set the computational domain as $\Omega = [0, 2\pi]^2$, and use the Legendre-Galerkin method to discretize the space. Each direction uses Legendre polynomials of degrees up to 1024.

4.2.1. Rotating Hele-Shaw cell

Rotating the Hele-Shaw cell is a common method used to obtain fingering patterns, which will be implemented in this example. Initially, the low-viscosity fluid (nematic phase) is set to occupy a small circular area in the area, and the outside



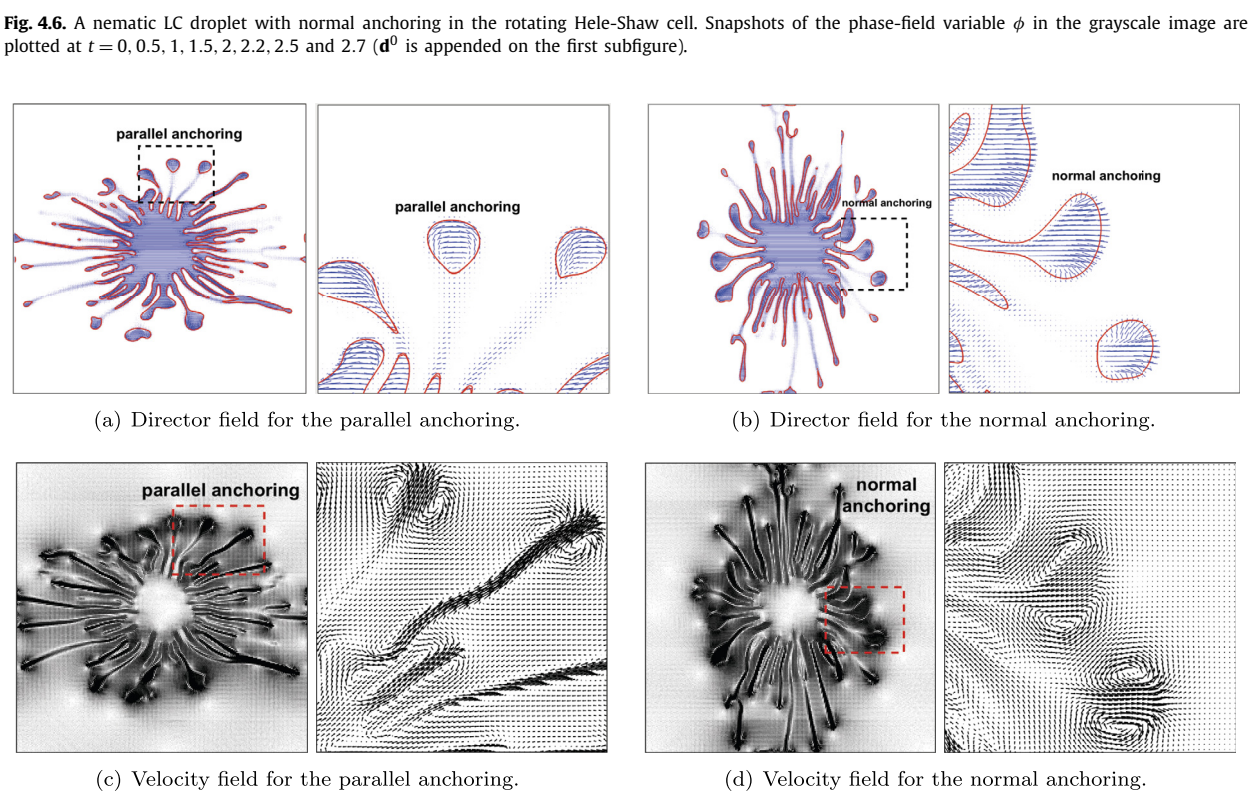
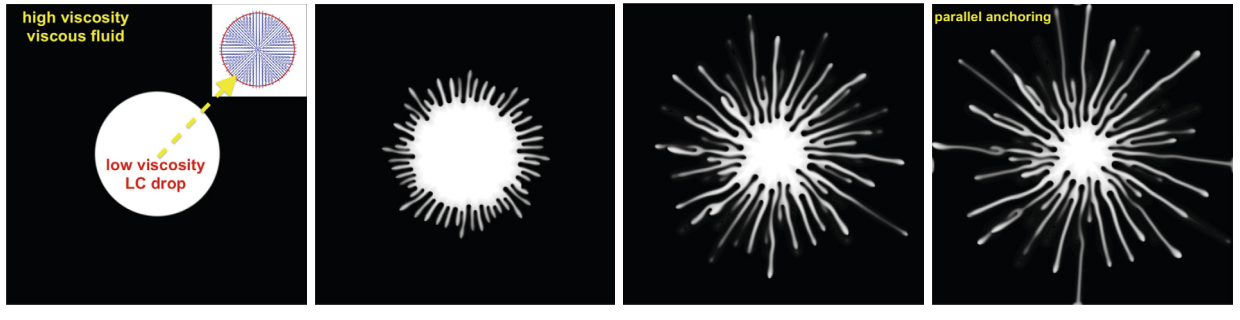


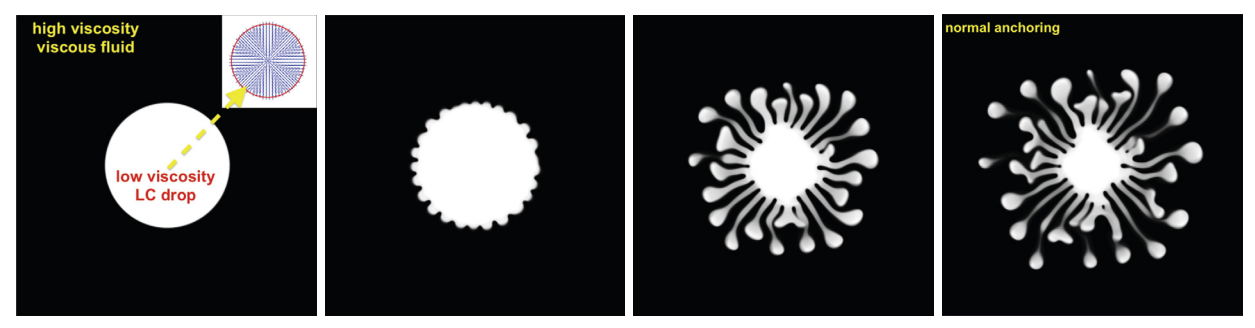
Fig. 4.7. For (a) parallel anchoring and (b) normal anchoring, the director field **d** at t = 2.7 is plotted where the contour line of $\{\phi = 1/2\}$ is superimposed. For (c) parallel anchoring and (d) normal anchoring, the velocity field \mathbf{u} at t = 2.5 is plotted. In each subfigure, the figure on the right is a close-up view of the rectangular region highlighted in the left figure.

is filled with high-viscosity fluid (Newtonian phase). The two fluids are immiscible. The rotation state can be realized by applying an external rotation force in the Darcy equation. Specifically, we replace the momentum equation (2.10) with the following form (see [2,15]):

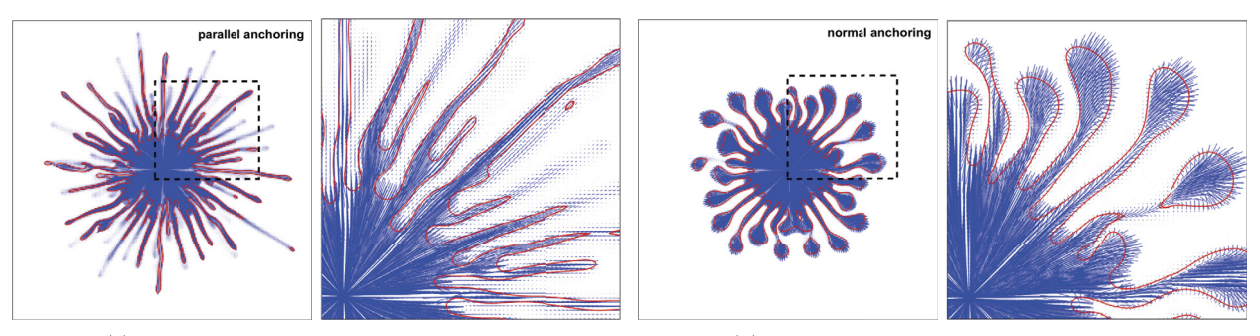
$$\tau \mathbf{u}_t + \beta \nu(\phi) \mathbf{u} + \nabla p = \boldsymbol{\omega} \nabla \mathbf{d} - \phi \nabla \mu + \nabla \cdot \sigma_e + \boldsymbol{f}_{rot}, \tag{4.3}$$



(a) ϕ at t = 0, 1, 2.5, 3 for parallel anchoring.



(b) ϕ at t = 0, 1, 2.5, 3 for normal anchoring.



(c) **d** at t = 2.5 for the parallel anchoring.

(d) \mathbf{d} at t = 2.5 for the normal anchoring.

Fig. 4.8. For (a) parallel anchoring and (b) normal anchoring, the phase-field variable ϕ at various times are plotted. For (c) parallel anchoring and (d) normal anchoring, the director field \mathbf{d} at t=2.5 is plotted. In the first subfigure of (a) and (b), the initial profile of \mathbf{d}^0 is attached in the small inset figure. In (c) and (d), the subfigure on the right is a close-up view of the rectangular region highlighted in the subfigure on the left.

where $\boldsymbol{f}_{rot} = \Upsilon_g \phi(\Upsilon_\omega^2 \boldsymbol{r} + 2\Upsilon_\omega(e_z \times \boldsymbol{u}))$ is the applied rotating force, $e_z = (0, 0, 1)$, $\boldsymbol{r} = \boldsymbol{x} - \boldsymbol{x}_0$, and Υ_g, Υ_w are constants given in (4.4).

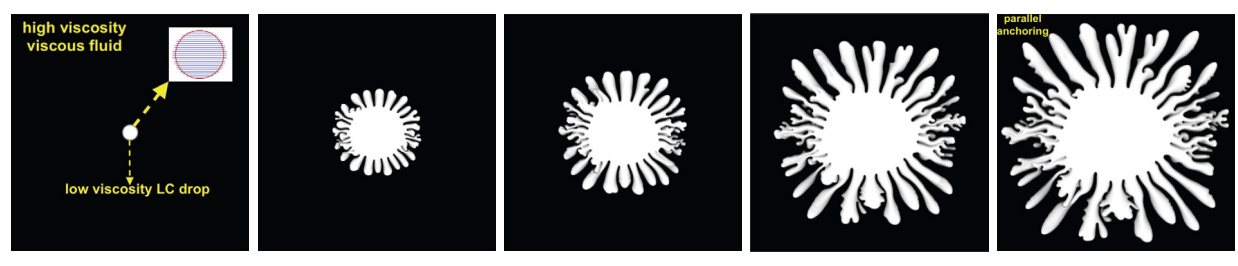
The initial condition is still from (4.1), and some small disturbances are imposed on the circumference of the initial droplet, i.e., $r_0=1.3+0.01 {\rm rand}(\textbf{x})$. The profile of ϕ^0 is shown in Fig. 4.4(a) which is drawn by using the grayscale image. We set the model parameters as

$$\begin{cases} \Upsilon_g = 5, \Upsilon_w = 5, \mathbf{x}_0 = (\pi, \pi), \\ M_1 = 0.01, \epsilon = 0.1, \lambda = 1e - 4, B = 1, s = 1.2, \phi_c = \frac{1}{2}, \\ M_2 = 10, K = 1e - 4, \nu_1 = 1, \nu_2 = 0.1, \eta = 0.01, \\ \tau = 1, \beta = 500, C = 0.02, S_1 = 4, S_2 = 0.02, \delta t = 1e - 4, \end{cases}$$

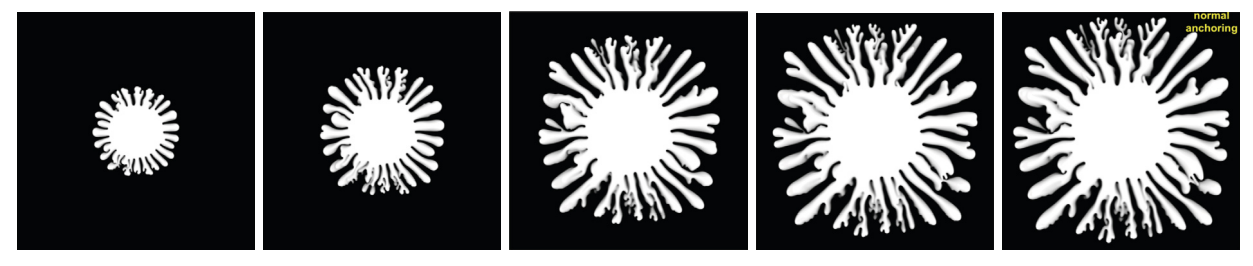
$$(4.4)$$

where v_1 is the high viscosity of the displaced fluid (Newtonian), v_2 is the low viscosity of the droplet (Nematic). We first conduct the simulation for the Newtonian-Newtonian case, i.e., the droplet and its surrounding fluid are both viscous Newtonian phase, and then study the pattern differences caused by the LC elastic energy for the Newtonian-Nematic case, i.e., the droplet is a nematic LC phase and its ambient fluid is a viscous Newtonian phase.

Fig. 4.4 exhibits the dynamical changes of the phase-field variable ϕ for the Newtonian-Newtonian case by setting $K = \alpha = \eta = 0$. Snapshots of ϕ at different times are drawn using the grayscale image. We observe that small protrusions appear



(a) ϕ at t = 0, 0.25, 0.5, 1, and 1.4 for parallel anchoring.



(b) ϕ at t = 0.25.0.5, 1, 1.25, and 1.4 for normal anchoring.

Fig. 4.9. Example of radial injection of nematic LC fluid for (a) parallel anchoring and (b) normal anchoring, where the initial condition of \mathbf{d}^0 is shown in the first subfigure of (a). In each subfigure, snapshots of the phase-field variable ϕ in the grayscale image are plotted at different times.

everywhere on the circumference of the droplet, and then evolve into many slender fingers, which become longer and longer as time goes by.

Then, the LC elastic effect is applied when the parameters K, α, η take the values given in (4.4). Two cases of anchoring conditions, parallel ($\gamma=1$) and normal ($\gamma=0$), are investigated respectively. Fig. 4.5 gives the snapshots of the phase-field variable ϕ at different times with parallel anchoring conditions. The resulting shape is significantly different from the case of viscous droplet. We observe that the initial protrusions are not around the droplet, but concentrate on the left and right ends of the droplet, and then spread to the other parts. Finally, the fingers formed at the left and right ends of the droplet are longer and thinner than the other parts. In Fig. 4.6, the normal anchoring condition is applied, and then the initial protrusions first appear on the top and bottom of the droplet. The fingers on the top and bottom are much longer and thinner than other parts. In Fig. 4.7, we plot the director field \mathbf{d} and the velocity field \mathbf{u} at t=2.7 for the two anchoring cases. It can be seen that the director field is parallel or perpendicular along with the droplet interface, and the contour of the velocity field is very consistent with the profiles of ϕ .

Below we further change the initial conditions of the director field \mathbf{d}^0 to observe different fingering patterns in the rotating Hele-Shaw cell. The initial condition of \mathbf{d}^0 (shown in the inset subfigure of the first subfigure in Fig. 4.8(a).) reads as

$$(\mathbf{d}_1^0, \mathbf{d}_2^0) = (\phi^0 \cos\theta, \phi^0 \sin\theta), \tag{4.5}$$

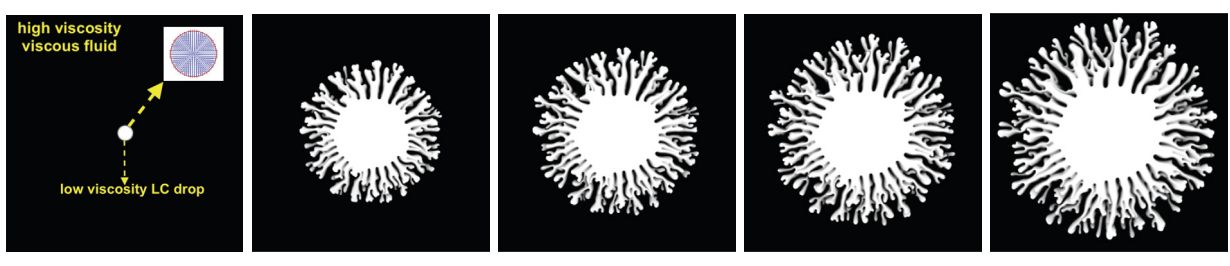
where $\theta = \arctan(\frac{y-\pi}{x-\pi+\epsilon_{\theta}})$ and $\epsilon_{\theta} = 0.001$ is used to ensure the denominator $x-\pi+\epsilon_{\theta}\neq 0$. Other initial conditions of ϕ , \mathbf{u} , p and the model parameters are the same as Fig. 4.5 and Fig. 4.6. Snapshots of ϕ at different times for parallel and normal anchoring conditions at various time are shown in Fig. 4.8(a) and (b), respectively. The parallel anchoring case produces a uniform and slender finger shape, while the fingering pattern of the normal anchoring produces a circular satellite droplet attached to the tip of each elongated finger. In Fig. 4.8(c)-(d), the director field \mathbf{d} at t=2.5 is plotted for the two anchoring cases, where we observe the parallel and vertical orientations along the droplet interface.

4.2.2. Radial injection of a less viscous fluid

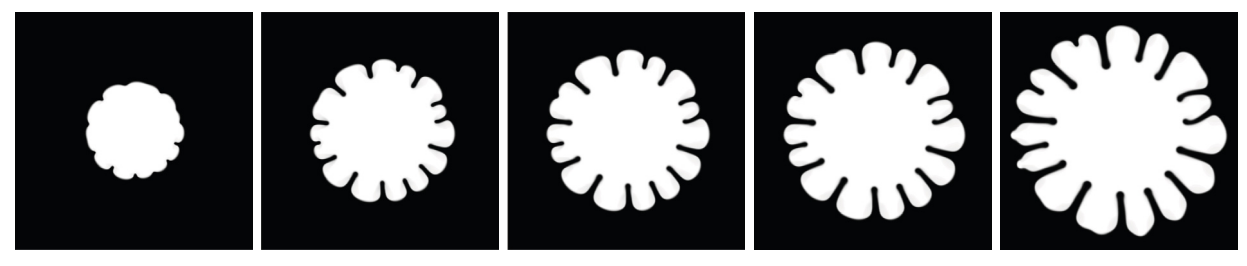
In the second numerical example, we simulate a radial injection of low-viscosity fluid (LC phase) to displace high-viscosity viscous fluid. We set the initial condition as a small circular piece of low-viscosity fluid located in the center of the domain, filled with high-viscosity viscous fluid on the outside (shown in the first subfigure of Fig. 4.9(a)), and then inject the low-viscosity fluid at a constant rate from the center. Physical and numerical experiments show that as the size of the fluid interface increases outward, fingers are formed, spread out and move in the direction of separation from each other, and finally get very complex branching patterns, see [1,3,9,16,18,25,49,53,54,63,64].

To represent the injection flow, we adopt the Gaussian method designed in [64] where a potential radial velocity \mathbf{u}_p is imposed in the momentum equation and the equations for ϕ and \mathbf{d} . Namely, the equations for ϕ , \mathbf{d} , and \mathbf{u} are modified as

$$\mathbf{d}_t + (\mathbf{u} + \mathbf{u}_p) \cdot \nabla \mathbf{d} + \frac{1 - s}{2} \mathbf{d} \nabla (\mathbf{u} + \mathbf{u}_p) - \frac{1 + s}{2} \mathbf{d} \cdot \nabla (\mathbf{u} + \mathbf{u}_p) = -M_1 \omega, \tag{4.6}$$



(a) ϕ at t = 0, 0.6, 0.8, 1, and 1.3 for parallel anchoring.



(b) ϕ at t = 0.4, 0.8, 1, 1.2, and 1.6 for normal anchoring.

Fig. 4.10. Example of radial injection of nematic LC fluid for (a) parallel anchoring and (b) normal anchoring, where the initial condition of \mathbf{d}^0 is shown in the first subfigure of (a). In each subfigure, snapshots of the phase-field variable ϕ in the grayscale image are plotted at different times.

$$\phi_t + \nabla \cdot (\mathbf{u}\phi) + (\mathbf{u}_p \cdot \nabla)\phi = M_2 \Delta \mu, \tag{4.7}$$

$$\tau \mathbf{u}_t + \beta \nu(\phi)(\mathbf{u} + \mathbf{u}_p) + \nabla p = \boldsymbol{\omega} \nabla \mathbf{d} - \phi \nabla \mu + \nabla \cdot \sigma_e, \tag{4.8}$$

where $\mathbf{u}_p = -C(1-e^{-4r^2/R_0^2})\tilde{\mathbf{r}}, r = \sqrt{(x-x_0)^2 + (y-y_0)^2}, \tilde{\mathbf{r}}(x,y) = (\frac{x-x_0}{r+\varepsilon}, \frac{y-y_0}{r+\varepsilon}), C$ is the injection strength, R_0 is the radius of the circular injection region, ε is a small quantity such that $r + \varepsilon \neq 0$. We still set the computational domain as $\Omega = [0, 2\pi]^2$ and the model parameters as

$$\begin{cases} M_1 = 0.01, \epsilon = 0.1, \lambda = 0.01, B = 1, s = 1.2, \phi_c = \frac{1}{2}, \\ M_2 = 1, K = 0.01, \alpha = 5, \nu_1 = 1, \nu_2 = 0.1, \gamma = 1, \eta = 0.01, \\ \tau = 1, \beta = 1000, C = 0.02, S_1 = 4, S_2 = 0.02, R_0 = 0.2, C = 0.65, \varepsilon = 1e - 3, \delta t = 1e - 4. \end{cases}$$

$$(4.9)$$

We first use the initial conditions give in (4.1) where $\tilde{r} = 0.2 + 0.01$ rand(\boldsymbol{x}), and study how different the fingering patterns are formed by different anchoring conditions. In Fig. 4.9(a) and (b), parallel and normal anchoring conditions are used respectively. Parallel anchoring results in the formation of finer finger-like structures at the left and right ends and more tiny sub-fingers, while normal anchoring will result in similar structures at the upper and lower ends. In Fig. 4.10(a) and (b), we change the initial orientation of \mathbf{d}^0 to the formulation given in (4.5). In this case, parallel anchoring and normal anchoring present completely different results. Parallel anchoring result in countless slender branches and sub-fingers, while normal anchoring conditions can only produce a few thick fingers.

5. Concluding remarks

We design an "ideal" numerical scheme to solve the highly complex nonlinear Darcy flow-coupled Newtonian-Nematic model. The scheme is called "ideal" since it is the first numerical scheme that enjoy so many desired properties at the same time, including second-order time accuracy, linearity, unconditional energy stability, and decoupling structure. The scheme is constructed based on a combination of a variety of effective numerical methods, including the projection method, quadratization method, as well as a new decoupling technique by designing some auxiliary ODEs with specific form. The detailed actual realization, solvability and rigorous proof of stability are given. Numerous numerical examples, including the tests of convergence and stability, and the benchmark fingering instability experiments caused by radial injection and rotating Hele-Shaw cell are simulated. Numerical results show that the initial orientation of the nematic liquid crystal and its elastic properties have an important influence on the fingering structure.

CRediT authorship contribution statement

Chuanjun Chen: Revise, algorithm implementation. **Xiaofeng Yang:** Algorithm development and implementation, writing, revise.

Declaration of competing interest

The authors declare that they have no known competing financial interests or personal relationships that could have appeared to influence the work reported in this paper.

Acknowledgements

The work of C. Chen was partially supported by the NSFC-11771375 and NSFC-11571297, Shandong Province Natural Science Foundation ZR2018MAQ008. The work of X. Yang was partially supported by National Science Foundation with grant number DMS-2012490.

References

- [1] S. Ahmadikhamsi, F. Golfier, C. Oltean, E. Lefèvre, S.A. Bahrani, Impact of surfactant addition on non-Newtonian fluid behavior during viscous fingering in Hele-Shaw cell, Phys. Fluids 32 (1) (2020) 012103.
- [2] E. Álvarez-Lacalle, J. Ortín, J. Casademunt, Low viscosity contrast fingering in a rotating Hele-Shaw cell, Phys. Fluids 16 (2004) 908-924.
- [3] E. Álvarez-Lacalle, J. Ortín, J. Casademunt, Relevance of dynamic wetting in viscous fingering patterns, Phys. Rev. E 74 (2006) 025302.
- [4] S. Badia, F. Guillén-Gónzalez, J.V. Gutiérrez-Santacreu, An overview on numerical analyses of nematic liquid crystal flows, Arch. Comput. Methods Eng. 18 (2011) 285.
- [5] J. Bear, Dynamics of Fluids in Porous Media, Courier Dover Publications, New York, 1988.
- [6] R. Becker, X. Feng, A. Prohl, Finite element approximations of the Ericksen-Leslie model for nematic liquid crystal flow, SIAM J. Numer. Anal. 46 (2008) 1704–1731.
- [7] I. Bischofberger, R. Ramachandran, S.R. Nagel, An island of stability in a sea of fingers: emergent global features of the viscous-flow instability, Soft Matter 11 (2015) 7428–7432.
- [8] A. Buka, P. Palffy-Muhoray, Stability of viscous fingering patterns in liquid crystals, Phys. Rev. A 36 (1987) 1527-1529.
- [9] A. Buka, P. Palffy-Muhoray, Z. Rácz, Viscous fingering in liquid crystals, Phys. Rev. A 36 (1987) 3984-3989.
- [10] Ll. Carrillo, F.X. Magdaleno, J. Casademunt, J. Ortín, Experiments in a rotating Hele-Shaw cell, Phys. Rev. E 54 (1996) 6260-6267.
- [11] S. Chandrasekhar, Liquid Crystals, Cambridge University Press, 1992.
- [12] C. Chen, X. Yang, Efficient numerical scheme for a dendritic solidification phase field model with melt convection, J. Comput. Phys. 388 (2019) 41-62.
- [13] C. Chen, X. Yang, Fast, provably unconditionally energy stable, and second-order accurate algorithms for the anisotropic Cahn-Hilliard model, Comput. Methods Appl. Mech. Eng. 351 (2019) 35–59.
- [14] C. Chen, X. Yang, Fully-discrete finite element numerical scheme with decoupling structure and energy stability for the Cahn-Hilliard phase-field model of two-phase incompressible flow system with variable density and viscosity, ESAIM: Math. Model. Numer. Anal. 55 (2021) 2323–2347.
- [15] C.-Y. Chen, Y.-S. Huang, J.A. Miranda, Diffuse-interface approach to rotating Hele-Shaw flows, Phys. Rev. E 84 (2011) 046302.
- [16] J.-D. Chen, Growth of radial viscous fingers in a Hele-Shaw cell, J. Fluid Mech. 201 (1989) 223-242.
- [17] K. Cheng, C. Wang, S.M. Wise, An energy stable BDF2 Fourier pseudo-spectral numerical scheme for the square phase field crystal equation, Commun. Comput. Phys. 26 (2019) 1335–1364.
- [18] J.Y.Y. Chui, P. de Anna, R. Juanes, Interface evolution during radial miscible viscous fingering, Phys. Rev. E 92 (2015) 041003.
- [19] P.G. de Gennes, J. Prost, The Physics of Liquid Crystals, Oxford University Press, 1993.
- [20] L. Dede, H. Garcke, K.F. Lam, A Hele-Shaw-Cahn-Hilliard model for incompressible two-phase flows with different densities, J. Math. Fluid Mech. 20 (2018) 531–567.
- [21] Q. Du, L. Ju, X. Li, Z. Qiao, Maximum bound principles for a class of semilinear parabolic equations and exponential time differencing schemes, SIAM Rev. 63 (2) (2021) 317–359.
- [22] Q. Du, R.A. Nicolaides, Numerical analysis of a continuum model of phase transition, SIAM J. Numer. Anal. 28 (1991) 1310-1322.
- [23] J.L. Ericksen, Anisotropic fluids, Arch. Ration. Mech. Anal. 4 (1960) 231–237.
- [24] J.L. Ericksen, Liquid crystals with variable degree of orientation, IMA Prepr. Ser. 559 (1989).
- [25] R. Farajzadeh, A.A. Eftekhari, H. Hajibeygi, S. Kahrobaei, J.M. van der Meer, S. Vincent-Bonnieu, W.R. Rossen, Simulation of instabilities and fingering in surfactant alternating gas (SAG) foam enhanced oil recovery, J. Nat. Gas Sci. Eng. 34 (2016) 1191–1204.
- [26] J.J. Feng, X. Chen, P. Yue, C. Zhou, Chapter 11, drop dynamics in complex fluids in the book of understanding soft condensed matter via modeling and computation, Ser. Soft Condens. Matter 3 (2010) 339–363.
- [27] J.J. Feng, C. Liu, J. Shen, P. Yue, An energetic variational formulation with phase field methods for interfacial dynamics of complex fluids: advantages and challenges, IMA Vol. Math. Appl. 140 (2005) 1–26.
- [28] J.J. Feng, C. Liu, J. Shen, P. Yue, Transient drop deformation upon startup of shear in viscoelastic fluids, Phys. Fluids 17 (2005) 123101.
- [29] F.C. Frank, On the theory of liquid crystals, Discuss. Faraday Soc. 25 (1958) 19-28.
- [30] H. Gomez, V.M. Calo, Y. Bazilevs, T.J.R. Hughes, Isogeometric analysis of the Cahn-Hilliard phase-field model, Comput. Methods Appl. Mech. Eng. 197 (2008) 4333–4352.
- [31] H. Gomez, Kristoffer G. van der Zee, Computational phase-field modeling, in: Encyclopedia of Computational Mechanics, second edition, John Wiley & Sons. Ltd. ISBN 978-1-119-00379-3. 2017.
- [32] F. Guillén González, J. Koko, A splitting in time scheme and augmented Lagrangian method for a nematic liquid crystal problem, J. Sci. Comput. 65 (2015) 1129–1144.
- [33] D. Han, X. Wang, A second order in time, uniquely solvable, unconditionally stable numerical scheme for Cahn–Hilliard–Navier–Stokes equation, J. Comput. Phys. 290 (2015) 139–156.
- [34] D. Han, X. Wang, Decoupled energy-law preserving numerical schemes for the Cahn-Hilliard-Darcy system, Numer. Methods Partial Differ. Equ. 32 (3) (2016) 936–954.
- [35] D. Han, X. Wang, A second order in time, decoupled, unconditionally stable numerical scheme for the Cahn–Hilliard–Darcy system, J. Sci. Comput. 14 (2018) 1210–1233.
- [36] V.K. Horváth, J. Kertész, T. Vicsek, Viscous fingering in a smectic liquid crystal, Europhys. Lett. 4 (1987) 1133.
- [37] T.Y. Hou, C. Liu, J.G. Liu, Multi-Scale Phenomena in Complex Fluids: Modeling, Analysis and Numerical Simulation, Series in Contemporary Applied Mathematics, Higher Education Press, 2009.
- [38] Z. Hu, S.M. Wise, C. Wang, J.S. Lowengrub, Stable and efficient finite difference nonlinear-multigrid schemes for the phase field crystal equation, J. Comput. Phys. 228 (2009) 5323–5339.
- [39] J. Huang, F. Lin, C. Wang, Regularity and existence of global solutions to the Ericksen Leslie system in R², Commun. Math. Phys. 331 (2014) 805–850.

- [40] I.-H. Huh. S. Kai. Electroconvection in nematic liquid crystals in Hele-Shaw cells. Phys. Rev. E 68 (Oct 2003) 042702.
- [41] K. Kruse, J.F. Joanny, F. Julicher, J. Prost, K. Sekimoto, Asters vortices and rotating spirals in active gels of polar filaments, Phys. Rev. Lett. 92 (2004) 078101
- [42] F.M. Leslie, Some constitutive equations for anisotropic fluids, Q. J. Mech. Appl. Math. 19 (1966) 357-370.
- [43] D. Li, Z. Qiao, On second order semi-implicit Fourier spectral methods for 2d Cahn-Hilliard equations, J. Sci. Comput. 70 (January 2017) 301-341.
- [44] X. Li, L. Ju, X. Meng, Convergence analysis of exponential time differencing schemes for the Cahn-Hilliard equation, Commun. Comput. Phys. 26 (2019) 1510–1529.
- [45] F. Lin, C. Wang, Recent developments of analysis for hydrodynamic flow of nematic liquid crystals, Philos. Trans. R. Soc. Lond. A, Math. Phys. Eng. Sci. 372 (2014) 20130361.
- [46] C. Liu, J. Shen, X. Yang, Dynamics of defect motion in nematic liquid crystal flow: modeling and numerical simulation, Commun. Comput. Phys. 2 (2007) 1184–1198.
- [47] C. Liu, N.J. Walkington, Approximation of liquid crystal flows, SIAM J. Numer. Anal. 37 (2000) 725-741.
- [48] M. Mata, C.J. García-Cervera, H.D. Ceniceros, Ordering kinetics of a conserved binary mixture with a nematic liquid crystal component, J. Non-Newton. Fluid Mech. 212 (2014) 18–27.
- [49] S. Mollaei, A.H. Darooneh, Spreading fingering instability and shrinking of a hydrosoluble surfactant on water, Exp. Therm. Fluid Sci. 86 (2017) 98-101.
- [50] D.A. Nield, A. Bejan, Convection in Porous Media, 2nd ed., Springer-Verlag, New York, 1999.
- [51] R.L. Nós, A.M. Roma, C.J. García-Cervera, H.D. Ceniceros, Three-dimensional coarsening dynamics of a conserved, nematic liquid crystal-isotropic fluid mixture. J. Non-Newton. Fluid Mech. 248 (2017) 62–73.
- [52] I. Romero, Thermodynamically consistent time stepping algorithms for nonlinear thermomechanical systems, Int. J. Numer. Methods Eng. 79 (2009) 706–732.
- [53] P.G. Saffman, G. Taylor, The penetration of a fluid into a porous medium or Hele-Shaw cell containing a more viscous liquid, Proc. R. Soc. Lond. A 245 (1958) 312–329.
- [54] V. Sharma, S. Nand, S. Pramanik, C.-Y. Chen, M. Mishra, Control of radial miscible viscous fingering, J. Fluid Mech. 884 (2020) A16.
- [55] J. Shen, C. Wang, S. Wang, S. Wang, Second-order convex splitting schemes for gradient flows with Ehrlich-Schwoebel type energy: application to thin film epitaxy, SIAM J. Numer. Anal. 50 (2012) 105–125.
- [56] J. Shen, J. Xu, J. Yang, A new class of efficient and robust energy stable schemes for gradient flows, SIAM Rev. 61 (2019) 474-506.
- [57] J. Shen, X. Yang, Numerical approximations of Allen-Cahn and Cahn-Hilliard equations, Discrete Contin. Dyn. Syst., Ser. A 28 (2010) 1669-1691.
- [58] J. Shen, X. Yang, Decoupled energy stable schemes for phase field models of two phase complex fluids, SIAM J. Sci. Comput. 36 (2014) B122-B145.
- [59] J. Shen, X. Yang, Decoupled energy stable schemes for phase field models of two phase complex fluids, SIAM J. Sci. Comput. 36 (1) (2014) 122-145.
- [60] J. Shen, X. Yang, Decoupled, energy stable schemes for phase-field models of two-phase incompressible flows, SIAM J. Numer. Anal. 53 (1) (2015) 279–296.
- [61] J. Shen, X. Yang, The IEQ and SAV approaches and their extensions for a class of highly nonlinear gradient flow systems, Contemp. Math. 754 (2020) 217–245.
- [62] E. Tjhung, D. Marenduzzo, M.E. Cates, Spontaneous symmetry breaking in active droplets provides a generic route to motility, Proc. Natl. Acad. Sci. 109 (31) (2012) 12381–12386.
- [63] T. Tóth-Katona, Á. Buka, Nematic-liquid-crystal-air interface in a radial Hele-Shaw cell: electric field effects, Phys. Rev. E 67 (2003) 041717.
- [64] R. Tsuzuki, Q. Li, Y. Nagatsu, C.-Y. Chen, Numerical study of immiscible viscous fingering in chemically reactive Hele-Shaw flows: production of surfactants, Phys. Rev. Fluids 4 (2019) 104003.
- [65] A.A. Verhoeff, H.N.W. Lekkerkerker, Droplet snap-off in fluids with nematic liquid crystalline ordering, New J. Phys. 14 (2012) 023010.
- [66] S.M. Wise, C. Wang, J.S. Lowengrub, An energy-stable and convergent finite-difference scheme for the phase field crystal equation, SIAM J. Numer. Anal. 47 (3) (2009) 2269–2288.
- [67] H. Wu, X. Xu, C. Liu, Asymptotic behavior for a nematic liquid crystal model with different kinematic transport properties, Calc. Var. Partial Differ. Equ. 45 (2011) 319–345.
- [68] X. Yang, Linear first and second order and unconditionally energy stable numerical schemes for the phase field model of homopolymer blends, J. Comput. Phys. 327 (2016) 294–316.
- [69] X. Yang, A new efficient fully-decoupled and second-order time-accurate scheme for Cahn-Hilliard phase-field model of three-phase incompressible flow, Comput. Methods Appl. Mech. Eng. 376 (2021) 13589.
- [70] X. Yang, A novel fully-decoupled scheme with second-order time accuracy and unconditional energy stability for the Navier-Stokes equations coupled with mass-conserved Allen-Cahn phase-field model of two-phase incompressible flow, Int. J. Numer. Methods Eng. 122 (2021) 1283–1306.
- [71] X. Yang, A novel fully-decoupled, second-order and energy stable numerical scheme of the conserved Allen-Cahn type flow-coupled binary surfactant model, Comput. Methods Appl. Mech. Eng. 373 (2021) 113502.
- [72] X. Yang, A novel fully-decoupled, second-order time-accurate, unconditionally energy stable scheme for a flow-coupled volume-conserved phase-field elastic bending energy model, J. Comput. Phys. 432 (2021) 110015.
- [73] X. Yang, Numerical approximations of the Navier-Stokes equation coupled with volume-conserved multi-phase-field vesicles system: fully-decoupled, linear, unconditionally energy stable and second-order time-accurate numerical scheme, Comput. Methods Appl. Mech. Eng. 375 (2021) 113600.
- [74] X. Yang, M.G. Forest, H. Li, C. Liu, J. Shen, Q. Wang, F. Chen, Modeling and simulations of drop pinch-off from liquid crystal filaments and the leaky liquid crystal faucet immersed in viscous fluids, J. Comput. Phys. 236 (2013) 1–14.
- [75] X. Yang, H. Yu, Efficient second order unconditionally stable schemes for a phase field moving contact line model using an invariant energy quadratization approach, SIAM J. Sci. Comput. 40 (2018) B889–B914.
- [76] X. Yang, J. Zhao, Q. Wang, J. Shen, Numerical approximations for a three components Cahn-Hilliard phase-field model based on the invariant energy quadratization method, Math. Models Methods Appl. Sci. 27 (2017) 1993–2030.
- [77] H. Yu, X. Yang, Decoupled energy stable schemes for phase field model with contact lines and variable densities, J. Comput. Phys. 334 (2017) 665–686.
- [78] P. Yue, J.J. Feng, C. Liu, J. Shen, A diffuse-interface method for simulating two-phase flows of complex fluids, J. Fluid Mech. 515 (2004) 293-317.
- [79] P. Yue, J.J. Feng, C. Liu, J. Shen, Diffuse-interface simulations of drop-coalescence and retraction in viscoelastic fluids, J. Non-Newton. Fluid Dyn. 129 (2005) 163–176.
- [80] P. Yue, J.J. Feng, C. Liu, J. Shen, Transient drop deformation upon startup of shear in viscoelastic fluids, Phys. Fluids 17 (2005) 123101.
- [81] P. Yue, J.J. Feng, C. Liu, J. Shen, Viscoelastic effects on drop deformation in steady shear, J. Fluid Mech. 540 (2005) 427–437.
- [82] G.-D. Zhang, X. He, X. Yang, A fully decoupled linearized finite element method with second-order temporal accuracy and unconditional energy stability for incompressible MHD equations, J. Comput. Phys. 448 (2022) 110752.
- [83] J. Zhang, X. Yang, Unconditionally energy stable large time stepping method for the L2-gradient flow based ternary phase-field model with precise nonlocal volume conservation, Comput. Methods Appl. Mech. Eng. 361 (2020) 112743.
- [84] J. Zhao, H. Li, Q. Wang, X. Yang, A linearly decoupled energy stable scheme for phase-field models of three-phase incompressible flows, J. Sci. Comput. 70 (2017) 1367–1389.
- [85] J. Zhao, Q. Wang, X. Yang, Numerical approximations to a new phase field model for immiscible mixtures of nematic liquid crystals and viscous fluids, Comput. Methods Appl. Mech. Eng. 310 (2016) 77–97.

- [86] J. Zhao, X. Yang, Y. Gong, Q. Wang, A novel linear second order unconditionally energy stable scheme for a hydrodynamic Q-tensor model of liquid crystals, Comput. Methods Appl. Mech. Eng. 318 (2017) 803–825.
- [87] J. Zhao, X. Yang, J. Li, Q. Wang, Energy stable numerical schemes for a hydrodynamic model of nematic liquid crystals, SIAM J. Sci. Comput. 38 (2016) A3264–A3290.
- [88] J. Zhao, X. Yang, J. Shen, Q. Wang, A decoupled energy stable scheme for a hydrodynamic phase-field model of mixtures of nematic liquid crystals and viscous fluids, J. Comput. Phys. 305 (2016) 539–556.
- [89] C. Zhou, P. Yue, J.J. Feng, Dynamic simulation of droplet interaction and self-assembly in a nematic liquid crystal, Langmuir 24 (2008) 3099-3110.
- [90] C. Zhou, P. Yue, J.J. Feng, C. Liu, J. Shen, Heart-shaped bubbles rising in anisotropic liquids, Phys. Fluids 19 (2007) 041703.